Title

Interruption of the intratumor CD8+ T cell:Treg crosstalk improves the efficacy of PD-1 immunotherapy

Journal

Cancer Cell, 42(6)

ISSN

1535-6108

Authors

Geels, Shannon N
Moshensky, Alexander
Sousa, Rachel S
et al.

Publication Date

2024-06-01

DOI

10.1016/j.ccell.2024.05.013

Cancer Cell

Article

Interruption of the intratumor CD8$^+$ T cell:Treg crosstalk improves the efficacy of PD-1 immunotherapy

Graphical abstract

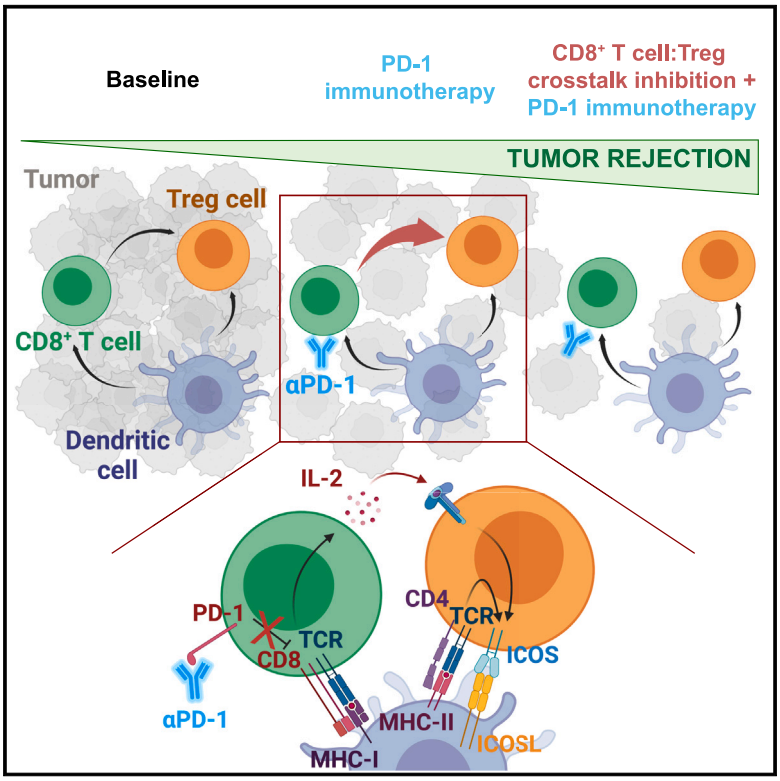

Authors

Shannon N. Geels, Alexander Moshensky, Rachel S. Sousa, ..., Anand K. Ganesan, Shivashankar Othy, Francesco Marangoni

Correspondence

f.marangoni@uci.edu

In brief

Understanding αPD-1-mediated immunosuppression is necessary to improve immunotherapy. Geels et al. reveal that tumor-Treg accrual after αPD-1 blockade does not depend on enhanced TCR signaling but on intratumor CD8$^+$ T cell:Treg communication via IL-2 and ICOS. Interruption of ICOS signaling increases the efficacy of PD-1 immunotherapy in melanoma.

Highlights

- PD-1 blockade expands Tregs in melanoma and limits the efficacy of immunotherapy
- Treg-intrinsic PD-1 inhibition does not cause tumor-Treg accumulation
- αPD-1 increases Treg numbers via an intratumor CD8$^+$ T cell/IL-2/ICOS axis
- Inhibition of the CD8$^+$T cell:Treg crosstalk by αICOSL synergizes with αPD-1 therapy

Geels et al., 2024, Cancer Cell *42*, 1051–1066
June 10, 2024
https://doi.org/10.1016/j.ccell.2024.05.013

CellPress

Cancer Cell

CellPress

Article

Interruption of the intratumor CD8+ T cell:Treg crosstalk improves the efficacy of PD-1 immunotherapy

Shannon N. Geels,[1,2] Alexander Moshensky,[1,2] Rachel S. Sousa,[1,3,4] Claire Murat,[1,2] Matias A. Bustos,[5] Benjamin L. Walker,[3,4] Rima Singh,[1,6] Stacey N. Harbour,[7] Giselle Gutierrez,[1] Michael Hwang,[1,2] Thorsten R. Mempel,[8] Casey T. Weaver,[7] Qing Nie,[3,4,9] Dave S.B. Hoon,[5] Anand K. Ganesan,[10] Shivashankar Othy,[1,2,11] and Francesco Marangoni[1,2,11,12,*]

[1]Institute for Immunology, University of California, Irvine, Irvine, CA, USA
[2]Department of Physiology and Biophysics, University of California, Irvine, Irvine, CA, USA
[3]Center for Complex Biological Systems, University of California, Irvine, Irvine, CA, USA
[4]NSF-Simons Center for Multiscale Cell Fate Research, University of California, Irvine, Irvine, CA, USA
[5]Department of Translational Molecular Medicine, Saint John's Cancer Institute, Santa Monica, CA, USA
[6]Department of Biological Chemistry, University of California, Irvine, Irvine, CA, USA
[7]Department of Pathology, University of Alabama, Birmingham, Birmingham, AL, USA
[8]Massachusetts General Hospital and Harvard Medical School, Boston, MA, USA
[9]Department of Developmental and Cell Biology, University of California, Irvine, Irvine, CA, USA
[10]Department of Dermatology, University of California, Irvine, Irvine, CA, USA
[11]Senior author
[12]Lead contact
*Correspondence: f.marangoni@uci.edu
https://doi.org/10.1016/j.ccell.2024.05.013

SUMMARY

PD-1 blockade unleashes potent antitumor activity in CD8+ T cells but can also promote immunosuppressive T regulatory (Treg) cells, which may worsen the response to immunotherapy. Tumor-Treg inhibition is a promising strategy to improve the efficacy of checkpoint blockade immunotherapy; however, our understanding of the mechanisms supporting tumor-Tregs during PD-1 immunotherapy is incomplete. Here, we show that PD-1 blockade increases tumor-Tregs in mouse models of melanoma and metastatic melanoma patients. Mechanistically, Treg accumulation is not caused by Treg-intrinsic inhibition of PD-1 signaling but depends on an indirect effect of activated CD8+ T cells. CD8+ T cells produce IL-2 and colocalize with Tregs in mouse and human melanomas. IL-2 upregulates the anti-apoptotic protein ICOS on tumor-Tregs, promoting their accumulation. Inhibition of ICOS signaling before PD-1 immunotherapy improves control over immunogenic melanoma. Thus, interrupting the intratumor CD8+ T cell:Treg crosstalk represents a strategy to enhance the therapeutic efficacy of PD-1 immunotherapy.

INTRODUCTION

Immunotherapy using checkpoint blockade revolutionized the management of previously incurable malignancies by extending overall and progression-free survival in patients with various metastatic cancers.[1–7] PD-1 inhibition is the foundation of most checkpoint immunotherapy strategies; however, the majority of patients either do not respond to this treatment or relapse.[8] Discovering the mechanisms underlying treatment failure is a prerequisite for designing more efficacious antitumor strategies based on PD-1 antagonism.

Engagement of PD-1 on activated T cells by PD-L1 and PD-L2 recruits Shp2 and other phosphatases to the immunological synapse, suppressing T cell receptor (TCR) and CD28 signaling.[9,10] The rationale of PD-1 immunotherapy is to unleash the antitumor function of effector T cells, especially CD8+ T cells,[11–13] by antibody-mediated interruption of PD-1 interaction with its ligands. However, the impact of PD-1 blockade on tumor immunity extends beyond the stimulation of effector T cells. αPD-1 antibodies likely modify the whole tumor immune environment by orchestrating cytokine and chemokine production and by directly binding to various PD-1-expressing cells, including immunosuppressive CD4+Foxp3+ T regulatory (Treg) cells.[14] Tregs respond to tumor-associated antigens in secondary lymphoid organs by upregulating chemokine receptors necessary for recruitment to non-lymphoid tissues, including tumors.[15] Tregs reencounter their cognate antigen during brief interactions with dendritic cells (DCs) in the tumor environment[16] and instruct local immune suppression.[17] Accordingly, Treg accumulation in tumors is

an adverse prognostic factor in multiple cancers, including melanoma.[18]

While widespread Treg depletion facilitates tumor rejection, it also triggers severe autoimmunity. Thus, it is critical to understand how PD-1 immunotherapy modulates tumor-Treg responses to locally inhibit their immunosuppressive function. PD-1 blockade may support Treg numbers and activation in gastro-esophageal cancer,[14] and higher PD-1 expression in Tregs compared to $CD8^+$ T cells predicts checkpoint immunotherapy failure.[19] However, the mechanisms by which PD-1 inhibition supports tumor-Tregs remain understudied.

Here, we investigated the causes of Treg expansion after PD-1 blockade using patient samples and mouse models, Treg-specific gene deletion, intravital microscopy, intercellular communication analysis, and multiparametric immunofluorescence. We found that PD-1 blockade increased tumor-Treg numbers in immunogenic tumors and that such expansion limited the efficacy of immunotherapy. Treg accumulation was not due to enhanced TCR signaling; instead, αPD-1-mediated activation of $CD8^+$ T cells indirectly promoted Treg increase. The intratumor $CD8^+$ T cell:Treg crosstalk was mediated by IL-2 and ICOS. Administration of αICOSL antibodies acted as an immune conditioning regimen for the tumor environment, which enhanced the effectiveness of subsequent PD-1 immunotherapy.

RESULTS

PD-1 blockade triggers intratumor mechanisms supporting Tregs

We sought to understand why tumor-Tregs are increased in patients treated with PD-1 immunotherapy.[14] We focused on melanoma because it is sensitive to PD-1 blockade, yet most patients do not respond to immunotherapy.[6] These characteristics are captured by the mouse melanoma cell line D4M-S, a derivative of D4M melanoma[20] engineered to express the SIINFEKL peptide.[21] The tumor-Treg increase in αPD-1-treated patients could be due to enhanced infiltration from circulation or the triggering of Treg-supporting immune reactions within the tumor environment. To understand the relative contribution of each mechanism, we treated D4M-S bearing mice with FTY720, an S1PR1 functional antagonist[22] that blocks lymphocyte egress from lymphoid organs.[23] FTY720 decreased Treg, $CD8^+$ T cells, and $CD4^+Foxp3^-$ T helper (Th) cells in the blood of tumor-bearing mice (Figures S1A and S1B) and within the tumor environment (Figure S1C). Moreover, a course of FTY720 started 12 h before the intravenous transfer of congenically labeled lymphocytes did not impair Treg recruitment to tumor-draining lymph nodes (tdLNs) but prevented their influx into the tumor (Figures S1D and S1E). Therefore, FTY720 blocks Treg recruitment to tumors by retaining these cells in lymph nodes.

We next studied the contribution of continuous influx versus intratumor expansion to Treg accumulation after PD-1 blockade. Following FTY720 administration and PD-1 immunotherapy, we observed increased tumor-Treg, $CD8^+$ T cell, and Th cell numbers. In the absence of FTY720, where both intratumor T cell expansion and influx from the circulation could occur, baseline tumor-Treg, $CD8^+$ T cells, and Th cells increased, but the αPD-1-mediated numerical expansion did not reach statistical significance (Figures S1F and S1G). Analysis of T cell fold increase after αPD-1 administration in the presence of FTY720 revealed that intratumor mechanisms preferentially support Tregs over Th and $CD8^+$ T cells (Figure S1H). Thus, intratumor expansion is crucial for Treg accumulation after PD-1 immunotherapy.

Tumor immunogenicity drives Treg accumulation during PD-1 blockade

To investigate whether immunogenicity supports αPD-1-mediated tumor-Treg increase, we compared T cell populations in the non-immunogenic parental line D4M[24] and immunogenic D4M-S melanomas treated with αPD-1 or isotype control antibodies (Figure 1A). We found that αPD-1 treatment did not change the numbers or percentages of Treg, $CD8^+$ T cells, and Th cells in D4M melanomas. Conversely, immunogenic D4M-S tumors had more Treg, Th, and $CD8^+$ T cells than D4M melanomas at baseline, and PD-1 blockade significantly enhanced $CD8^+$ T cell and Treg counts (Figures 1B–1D, S1I, and S1J). In D4M-S melanomas, the administration of αPD-1 increased proliferation (Figures 1E, 1F, and S1K), IFNγ, and TNF production by $CD8^+$ T cells (Figure S1L). Granzyme B expression remained unchanged (Figure S1M). Notably, PD-1 inhibition did not significantly increase Treg proliferation (Figures 1E, 1F, and S1K) but caused the upregulation of Foxp3 and the activation markers GITR and ICOS (Figure 1G). Similar results were obtained using the immunogenic MC38 colon carcinoma (Figures S1N–S1P). Altogether, these data show that PD-1 inhibition leads to elevated Treg numbers and expression of activation markers, not accompanied by increased proliferation, in two distinct immunogenic tumor models.

We then studied αPD-1-mediated Treg activation in tdLNs. There, Tregs exist in a resting state characterized by the $CD44^{lo}CD62L^+$ phenotype ("central" or cTregs) and a $CD44^{hi}$ $CD62L^-$ activated state ("effector" or eTregs).[25] The numbers of lymph node Treg, $CD8^+$ T cells, and Th cells increased with αPD-1 treatment, irrespective of tumor immunogenicity. The percentage of $CD8^+$ T cells and Th cells was unchanged. Still, there was a trend toward increased Treg percentages after PD-1 blockade (Figures S1Q–S1S), possibly due to PD-1-mediated restriction of lymph node Treg activation at homeostasis.[26] eTregs and activated $CD44^{hi}CD62L^-$ $CD8^+$ T cells showed a tendency to accumulate after PD-1 blockade (Figure S1T), accompanied by increased proliferation (Figure S1U). PD-1 blockade did not change the expression of Foxp3, GITR, and ICOS in lymph node eTregs (Figure S1V). Thus, unlike in tumors, PD-1 inhibition induces lymph node Treg proliferation without increased expression of activation markers. Radiation chimeras reconstituted with a 1:1 mixture of wild type and *Pdcd1*$^{-/-}$ bone marrow showed equal representation of wild-type and PD-1-sufficient cTreg in tdLNs, while eTregs were skewed toward PD-1-deficient cells. Thus, PD-1 inhibition promotes cTreg to eTreg transition in lymph nodes. However, the percentage of *Pdcd1*$^{-/-}$ Tregs in tumors and *Pdcd1*$^{-/-}$ eTregs in lymph nodes was comparable (approximately 70%), indicating that the ratio of PD-1-deficient to wild-type Tregs was established within lymph node eTregs, which subsequently migrated to the tumor. These data also revealed that PD-1 inhibition does not confer a competitive

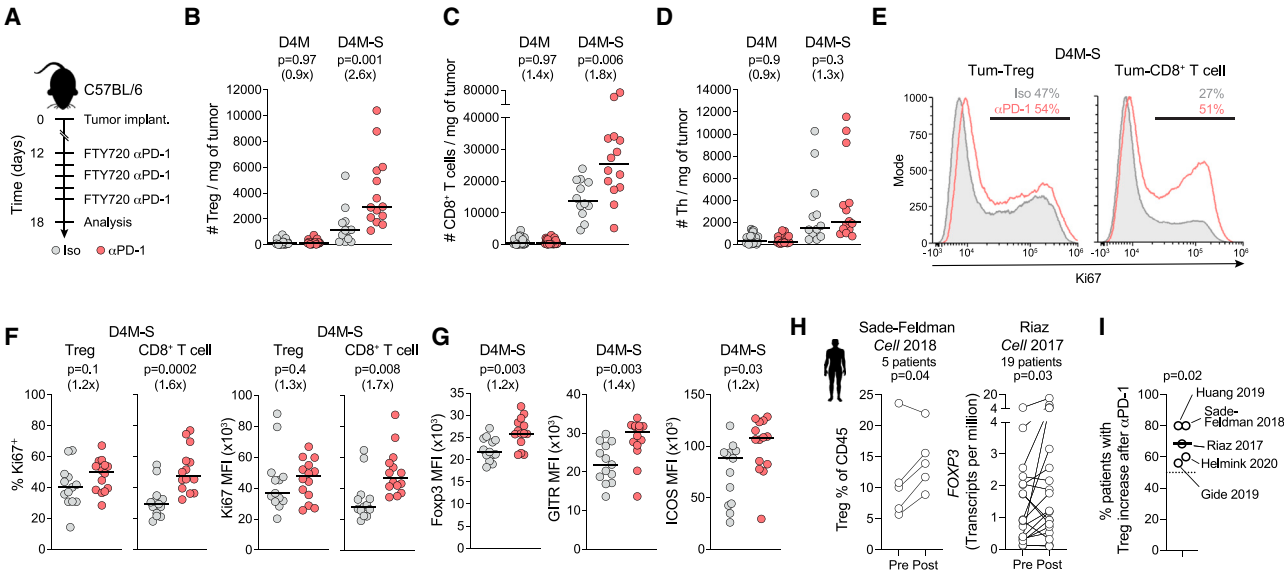

Figure 1. PD-1 blockade increases tumor-Treg counts

(A) Scheme to assess the impact of αPD-1 on tumor T cells.

(B–D) Treg (B), CD8$^+$ T cell (C), and Th cell (D) numbers per mg of tumor in mice bearing D4M or D4M-S melanomas ± αPD-1.

(E and F) Histograms (E) and Ki67 quantification (F) in tumor-Treg and CD8$^+$ T cells.

(G) Foxp3, GITR, and ICOS MFI in tumor-Tregs. For B–G, n = 25 (D4M) and 12–14 (D4M-S) mice/group from 5 (D4M) or 3 (D4M-S) experiments. Bars depict medians. p values by Mann-Whitney U test.

(H) Treg quantification in the indicated datasets. p values by paired Student's t test.

(I) Comparison of patients with increased Tregs after PD-1 blockade in the indicated datasets. p value by one-sample t test against the theoretical value of 50%. The solid bar represents the mean.

See also Figure S1.

advantage to Tregs after they enter the tumor environment (Figures S1W and S1X). Together, our findings indicate that the consequences of PD-1 inhibition for lymph nodes and tumor-Tregs are different.

PD-1 immunotherapy increases Tregs in human melanoma

To extend our observations to humans, we conducted a meta-analysis of tumor-Tregs in metastatic melanoma patients treated with PD-1 monotherapy. We compiled publicly available datasets encompassing single-cell RNA sequencing,[13] bulk RNA sequencing,[27–29] and immunofluorescence.[30] We reanalyzed these data to compare Treg levels in the same patients before and after PD-1 monotherapy. Paired Treg analysis revealed a statistical increase in the single-cell RNA sequencing dataset[13] and one of the bulk RNA sequencing datasets[27] (Figure 1H). Treg increase did not reach statistical significance in the other two bulk RNA sequencing datasets[28,29] (Figure S1Y). When the five datasets were analyzed together, the proportion of patients with tumor-Treg accumulation after PD-1 monotherapy was significantly higher than the theoretical value of 50%, corresponding to no increase (Figure 1I). Thus, our meta-analysis of 53 metastatic melanoma patients with pre- and post-PD-1 immunotherapy biopsies suggests that the majority experienced Treg increase after treatment. Consequently, we sought to understand the relevance and mechanistic underpinnings of αPD-1-mediated Treg expansion in melanoma.

αPD-1-mediated increase in tumor-Treg numbers restricts immunotherapy efficacy

While PD-1 immunotherapy synergizes with extensive Treg depletion,[31–33] a causal link between the αPD-1-mediated Treg increase and the outcome of immunotherapy has not been established. To address this question, we administered αPD-1 to D4M-S melanoma-bearing *Foxp3^{DTR}* mice, decreased Treg numbers to pre-therapy levels using an accurately titrated (not shown) dose of diphtheria toxin (DT), and measured tumor weight (Figure 2A). PD-1 inhibition increased tumor-Tregs compared to isotype-treated mice. Co-administration of DT and αPD-1 reduced Treg percentages to the level of the isotype group in 13/27 (Treg Low) mice and was ineffective on the remaining mice (Treg Hi) (Figures 2B, S2A, and S2B). After αPD-1 treatment, 30% of mice showed unrestricted tumor growth, while the remaining mice controlled it (Figure 2C). Importantly, we observed that 43% of Treg Hi mice experienced unrestricted tumor growth compared to 8% in the Treg Low group (Figure 2C). These data indicate that PD-1-mediated tumor-Treg increase hinders tumor rejection.

An indirect mechanism drives tumor-Treg accumulation after PD-1 immunotherapy

We hypothesized that tumor-Treg accumulation following αPD-1 was due to enhanced TCR activation. Because TCR signaling induces Ca^{2+} influx in T cells, we monitored the levels of Ca^{2+} ions using the genetically encoded indicator Salsa6f, a fusion of tdTomato and GCaMP6f. TdTomato emits constant red

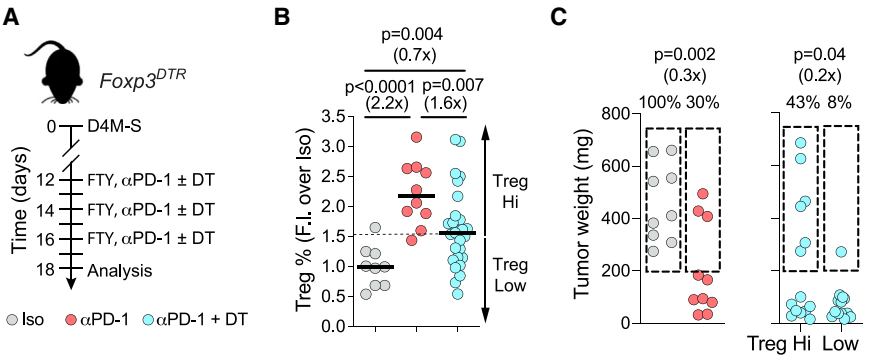

Figure 2. αPD-1-mediated Treg increase hinders tumor rejection

(A) Scheme for partial Treg ablation.

(B) Tumor-Treg fold increase over the isotype group. The dotted line indicates the threshold for increased Tregs (the mean between the highest isotype and lowest αPD-1 sample values). *n* = 9 (Iso) 10 (αPD-1) and 27 (αPD-1+DT) mice/group from two experiments. Bars depict the median value of the distribution. *p* values by Mann-Whitney U test.

(C) Tumor weight in mice treated as indicated. Mice treated with αPD-1+DT were stratified by Treg Hi (*n* = 14) and Low (*n* = 13). Rectangles indicate the tumor weight range in isotype-treated animals. *p* values by chi-squared test.

See also Figure S2.

fluorescence, whereas green fluorescence from GCaMP6f is proportional to the cytosolic concentration of Ca^{2+}.[34] We bred *Foxp3*^{creERT2}x*Rosa26*$^{LSL\text{-}Salsa6f}$ mice that express Salsa6f specifically in Tregs upon tamoxifen administration (Figure 3A). To quantify tumor-Treg activation *in vivo*, we implanted a D4M-S tumor in tamoxifen-treated *Foxp3*^{creERT2}x*Rosa26*$^{LSL\text{-}Salsa6f}$ mice. Upon tumor establishment, we installed a dorsal skinfold chamber (DSFC) enabling optical access to the cancer and performed functional intravital microscopy (F-IVM) (Figure 3B). We distinguished resting and activated tumor-Tregs based on Salsa6f red and green fluorescence signals (Figure S3A and Video S1). Tregs were frequently activated in both control mice and mice treated with αPD-1 24 h earlier (Figure 3C and Video S2). For each cell track, we quantified the GFP intensity over time and subtracted the baseline signal. We identified several peaks of GFP fluorescence, corresponding to individual instances of activation (Figure 3D). Approximately 30% of endogenous Tregs in both groups signaled during the observation window (Figure 3E), in line with previous findings.[16] To quantify activation, we focused on track segments corresponding to signaling peaks (Figure 3F). The percentage of time an individual Treg was observed signaling was equivalent in control and αPD-1-treated mice (Figure 3G). The maximum fluorescence increased while signaling duration decreased in the αPD-1 group, resulting in a comparable area under the curve (AUC) between control and αPD-1-treated mice (Figure 3H).

To investigate whether these slight variations in signaling dynamics imposed by αPD-1 treatment correlated with increased TCR-mediated Treg activation, we quantified Zap70 and Akt phosphorylation without further *in vitro* restimulation (Figure 3I). We found higher Zap70 phosphorylation in tumor-Tregs after αPD-1 treatment compared to isotype-treated animals and phosphatase-treated technical controls (Figure 3J). However, the level of Zap70 phosphorylation in Tregs was lower than in tumor $CD8^+$ T cells (Figure 3K). Akt phosphorylation was significantly increased in $CD8^+$ T cells but not Tregs. These data are consistent with $CD8^+$ T cells being the primary target of PD-1 immunotherapy.[12,13] To study whether the moderate increase in TCR signaling in Tregs could be responsible for their intratumor accumulation, we generated *Foxp3*^{creERT2}x*Pdcd1*$^{f/f}$ mice to selectively delete PD-1 on Tregs by tamoxifen administration (Figure 3L). The efficiency of PD-1 deletion was ~80% (Figure 3M). In agreement with our phospho-flow data, we observed only a slight increase in Ki67 expression in PD-1-deleted compared to PD-1-sufficient Tregs in the same mouse, even when excluding $CD44^{lo}$ Tregs that were Ki67 negative and may not have responded to tumor-associated antigens. GITR and ICOS remained unchanged (Figure S3B). Importantly, Treg-specific PD-1 deletion alone did not increase tumor-Treg numbers compared to control *Foxp3*^{creERT2} mice (Figure 3N), demonstrating that the modest enhancement of TCR-mediated Treg activation following PD-1 blockade is insufficient to promote intratumor Treg accumulation. In contrast, antibody-mediated PD-1 inhibition increased Treg numbers, even in mice bearing PD-1-deleted tumor-Tregs (Figure 3N). Therefore, while PD-1 blockade elicits cell-intrinsic and -extrinsic mechanisms supporting tumor-Tregs, only the latter explains Treg accumulation within the tumor.

$CD8^+$ T cells and IL-2 are required for αPD-1-mediated tumor-Treg accumulation

Considering the pronounced response of $CD8^+$ T cells to αPD-1, we hypothesized that $CD8^+$ T cells support tumor-Treg accumulation during PD-1 blockade. Analysis of D4M-S tumors explanted from *Foxp3*^{GFP}x*E8I*^{cre}x*Rosa26*$^{LSL\text{-}Tomato}$ mice showed several clusters of $CD8^+$ T cells and Tregs (Figure 4A). To assess colocalization, we measured the distance between each Treg and the closest $CD8^+$ T cell in the original dataset and after randomization of Treg positions (Figure S4A). The median distance between Treg and $CD8^+$ T cells in the original dataset was significantly lower (10 μm) than the distance after Treg shuffling (15 μm), demonstrating a non-random distribution of Tregs relative to $CD8^+$ T cells (Figure 4B). Importantly, the depletion of $CD8^+$ T cells during αPD-1 therapy completely prevented Treg accumulation in tumors (Figures 4C and 4D) but not in tdLNs (Figure S4B).

Since αPD-1 only marginally enhanced tumor-Treg proliferation (Figures 1E and 1F) and Treg recruitment from the circulation was blocked by FTY720, we posited that αPD-1-stimulated $CD8^+$ T cells decrease Treg apoptosis. Indeed, the quantification of active caspase-3/7 showed that PD-1 immunotherapy significantly reduced apoptosis in tumor-Tregs in a $CD8^+$ T cell-dependent manner (Figure 4E). We further hypothesized that the $CD8^+$ T cell-derived molecule supporting tumor-Tregs was IL-2, as it is a crucial trophic and survival factor for Tregs,[25,35,36] and a recent report showed IL-2 production by

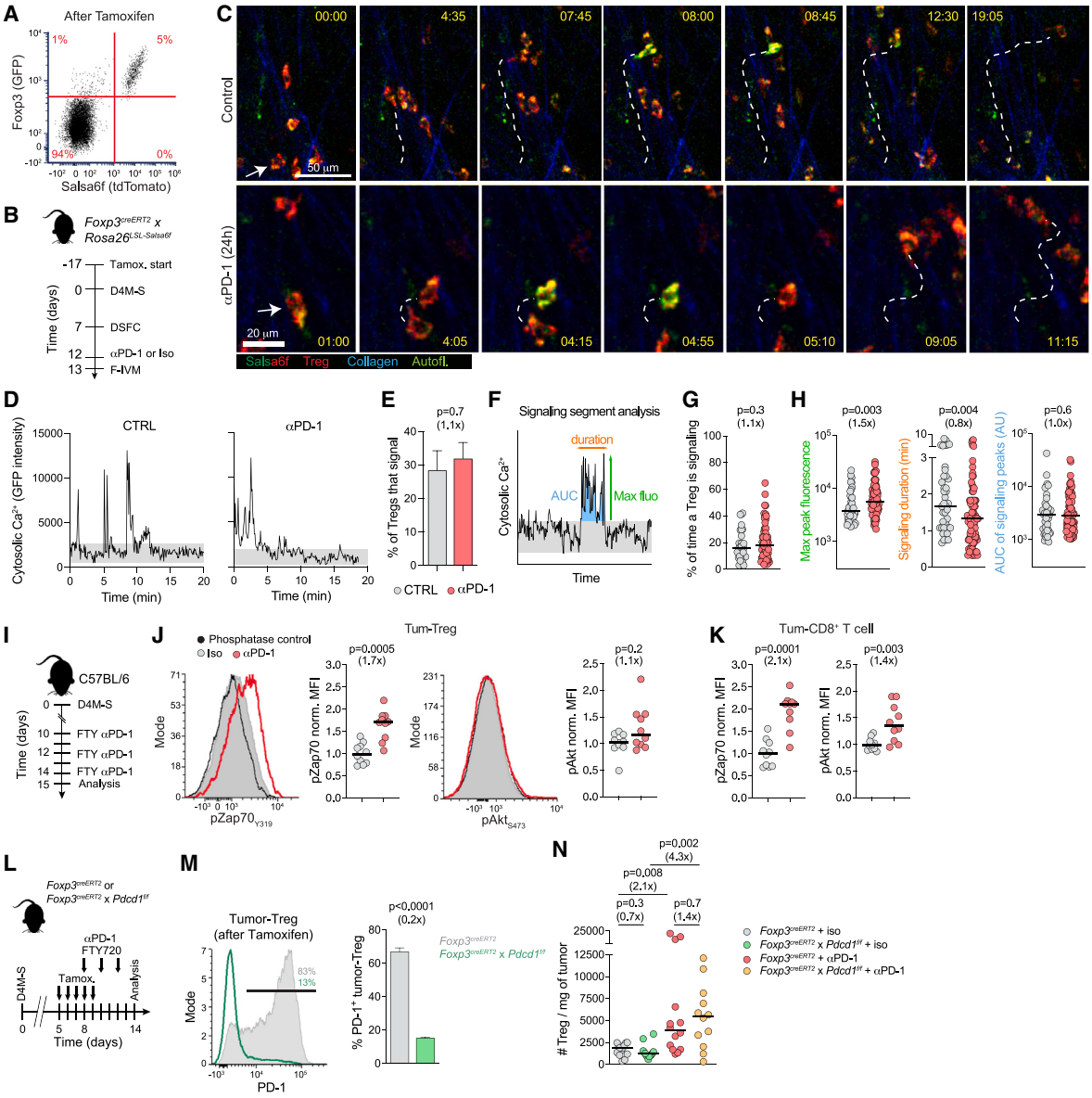

Figure 3. Indirect mechanisms drive tumor-Treg accumulation after PD-1 blockade

(A) Salsa6f expression in lymph node Tregs from a representative tamoxifen-treated *Foxp3*^{creERT2}x*Rosa26*$^{LSL\text{-}Salsa6f}$ mouse.

(B) Scheme for F-IVM.

(C) Image sequences illustrating tumor-Treg motility and Ca^{2+} signaling reported by Salsa6f, with or without αPD-1. Arrows and dotted lines highlight the tracked Tregs. Time in min:sec.

(D) GFP intensity in representative Treg tracks. The track-specific baseline is depicted in gray.

(E) Percentage of Treg tracks displaying at least one signaling peak. Mean ± SEM is shown. *p* values by Student's t test.

(F) Illustration of track segments and associated parameters.

(G) Percentage of time a Treg is signaling.

(H) Quantification of maximum GFP fluorescence, signaling duration, and AUC for individual signaling segments. For C–H, we analyzed 5 control and 7 αPD-1 movies, corresponding to 115 control and 207 αPD-1 Treg tracks and 41 control and 86 αPD-1 signaling segments.

(I) Scheme of phospho-flow cytometry.

(J and K) Representative histograms and quantification of pZap70 and pAkt in Tregs (J) and CD8$^+$ T cells (K) from D4M-S tumors ± PD-1 blockade. *n* = 10 mice/group from two experiments.

(L) Scheme of Treg-specific PD-1 deletion experiments.

(M) Quantification of PD-1 expression in tumor-Tregs within tamoxifen-treated *Foxp3*^{creERT2} or *Foxp3*^{creERT2}x*Pdcd1*$^{f/f}$ mice. Mean ± SEM is depicted. *p* values by Student's t test.

(N) Tumor-Treg counts in *Foxp3*^{creERT2} or *Foxp3*^{creERT2}x*Pdcd1*$^{f/f}$ mice ± αPD-1 treatment. *n* = 12 to 14 mice/group from three independent experiments. In G, H, J, K, and N, bars represent medians, and *p* values are calculated by Mann-Whitney U test.

See also Figure S3 and Videos S1 and S2.

Tcf7-expressing CD8$^+$ memory T cells during viral infection.[37] Moreover, *Tcf7*-expressing CD8$^+$ T cells infiltrate tumors and are exquisitely responsive to PD-1 immunotherapy.[38] To examine whether CD8$^+$ T cells can be an intratumor source of IL-2, we implanted D4M-S tumors into *Il2*^{GFP} mice[39] to identify IL-2-transcribing cells by GFP expression (Figure 4F). In line with previous studies,[40,41] the main source of IL-2 in lymph nodes were Th cells, while CD8$^+$ T cells only accounted for ~20% of IL-2-producing cells. In contrast, CD8$^+$ T cells were the primary producer of IL-2 in the tumor (~90% of IL-2-producing cells) independently of PD-1 blockade (Figures 4G and 4H). The analysis of IL-2 protein production by tumor CD8$^+$ T cells after αPD-1 (Figure 4I) showed no significant increase in the percentage of CD8$^+$ T cells producing IL-2 (Figures 4J and S4C). However, PD-1 blockade triggered the expansion of tumor CD8$^+$ T cells and, consequently, increased the numbers of IL-2-producing CD8$^+$ T cells (Figure 4K). To investigate if IL-2 is required for tumor-Treg accumulation after αPD-1, we blocked IL-2 binding to the α and β subunits of its receptor through neutralizing antibodies. We used *Foxp3*^{creERT2}x*Pdcd1*$^{f/f}$ mice to focus our analysis on indirect mechanisms elicited by PD-1 immunotherapy (Figure 4L). αPD-1-mediated tumor-Treg accumulation was entirely abrogated by IL-2 neutralizing antibodies (Figure 4M). IL-2 neutralization significantly reduced Ki67 expression in tumor-Tregs irrespective of αPD-1 treatment, confirming the critical role of IL-2 in tumor-Treg homeostasis.[16] However, changes in Treg proliferation upon αPD-1 treatment did not correlate with increased Treg numbers: PD-1 blockade alone led to tumor-Treg accumulation without Ki67 upregulation, while concomitant PD-1 inhibition and IL-2 neutralization failed to expand Tregs despite increased Ki67 expression (Figure 4M). Moreover, Treg expansion in tdLN after PD-1 blockade partially depended on IL-2 (Figure S4D), but Treg proliferation did not. (Figure S4E). This lack of correlation between Treg proliferation and accumulation suggests that other mechanisms, including modulation of apoptosis, play an important role in Treg accrual. Although combining IL-2 neutralization with PD-1 immunotherapy limited Treg expansion, it is not a viable antitumor strategy since IL-2 also supported tumor-associated CD8$^+$ T cells (Figure 4N). To test whether the lack of accumulation of PD-1-deficient tumor-Tregs in the absence of αPD-1 antibodies (Figure 3N) was due to limited IL-2, we treated tumor-bearing *Foxp3*^{creERT2}x*Pdcd1*$^{f/f}$ mice with IL-2 immunocomplexes (IL-2i.c.) that direct the effects of IL-2 to IL-2Rα-expressing cells[42] (Figure 4O). IL-2i.c. injection into mice bearing PD-1-deficient Tregs increased tumor-Tregs (Figure 4P). Together, these data demonstrate that IL-2 is necessary and sufficient for the intratumor expansion of PD-1-deficient Tregs. While we cannot exclude a role for Th-derived IL-2, our data indicate that CD8$^+$ T cells, the most abundant lymphocyte in D4M-S melanomas (Figures 1A–1D), are a source of IL-2 sufficient to support Tregs within the tumor environment.

αPD-1-mediated tumor-Treg accumulation depends on TCR and CD28 signaling

In vitro studies proposed that IL-2 and CD28 may drive Treg expansion in the absence of TCR-mediated signaling.[43,44] If TCR-independent tumor-Treg accumulation occurred after PD-1 blockade, bystander Tregs with no specificity for tumor antigens might participate in local immunosuppression. We investigated this possibility by counting tumor-Tregs in mice with Treg-specific, inducible deletion of either TCRα or CD28 (*Foxp3*^{creERT2}x*Trac*$^{f/f}$ or *Foxp3*^{creERT2}x*Cd28*$^{f/f}$). These mice received D4M-S tumors, tamoxifen, and αPD-1 before tumor-Treg analysis (Figure S4F). TCR deletion was ~70%, and CD28 deletion was ~55% (Figures S4G and S4H). Because TCR or CD28 deletion was incomplete, we performed subsequent analyses by gating on Tregs that were negative for these proteins. While PD-1 blockade in *Foxp3*^{creERT2} mice increased tumor-Treg levels 2-fold compared to isotype controls, Tregs negative for the TCR or CD28 failed to expand (Figure S4I). These data demonstrate that TCR and CD28 signaling are required for αPD-1-driven, CD8$^+$ T cell- and IL-2-dependent expansion of tumor-Tregs.

IL-2-mediated tumor-Treg accumulation depends on ICOS

To study the effect of IL-2 on tumor-Tregs, we administered IL-2i.c. to mice bearing D4M melanoma since this tumor contains fewer Tregs, and thus the effects of IL-2i.c. may be the most evident (Figure 5A). Tumor-Treg numbers were increased in response to αPD-1 and IL-2i.c., compared to αPD-1 only (Figure 5B). IL-2i.c. caused tumor-Treg expansion even in the absence of αPD-1 (Figure S5A), indicating that PD-1 blockade is not a prerequisite for Treg responsiveness to IL-2. Tumor-Treg accumulation was likely due to decreased apoptosis since proliferation was unchanged (Figures 5C and S5B), and influx from lymph nodes was blocked by FTY720. In addition, the expression of pro-apoptotic Bim increased after IL-2i.c. administration (Figure 5D), leading us to consider the IL-2-dependent anti-apoptotic factors Bcl-2, Bcl-xL, and Mcl-1 as possible molecules prolonging tumor-Treg survival. This mechanism would be reminiscent of lymph node cTregs, where high amounts of Bim are balanced by high Bcl-2 expression (Figure S5C). However, Bcl-2, Bcl-xL, and Mcl-1 were not upregulated in tumor-Tregs after treatment with αPD-1 and IL-2i.c. compared to αPD-1 alone (Figure 5E). IL-2i.c. treatment instead increased the expression of the costimulatory and anti-apoptotic molecule ICOS (Figures 5F and S5D). We thus inhibited ICOS signaling using antibodies blocking its only ligand ICOSL.[25] ICOSL inhibition prevented IL-2-mediated tumor-Treg accumulation (Figures 5G and 5H). Analysis of caspase-3/7 activation on freshly isolated tumor-Tregs showed that combining IL-2i.c. with PD-1 blockade decreased Treg apoptosis. αICOSL abolished this effect as the difference between αPD-1 alone and αPD-1 combined with IL-2i.c. and αICOSL was not significant (Figure S5E). Our results concur with previous studies demonstrating an anti-apoptotic role for ICOS signaling.[25,45–47] Similar to D4M melanomas, treatment of immunogenic D4M-S tumors with αPD-1 and IL-2i.c. did not modulate Ki67, Bcl-2, Bcl-xL, or Mcl-1 but increased ICOS expression on tumor-Tregs. ICOSL blockade counteracted IL-2i.c.-dependent tumor-Treg accumulation (Figures S5F–S5J). We also observed that αPD-1-mediated ICOS expression on tumor-Tregs depended on CD8$^+$ T cells (Figure 5I and 5J). Finally, we investigated whether ICOS controls tumor-Treg abundance through a Treg-intrinsic or -extrinsic mechanism. We generated bone marrow chimeras bearing a 1:1 mix of *Icos*$^{-/-}$ and DT receptor (DTR)-expressing

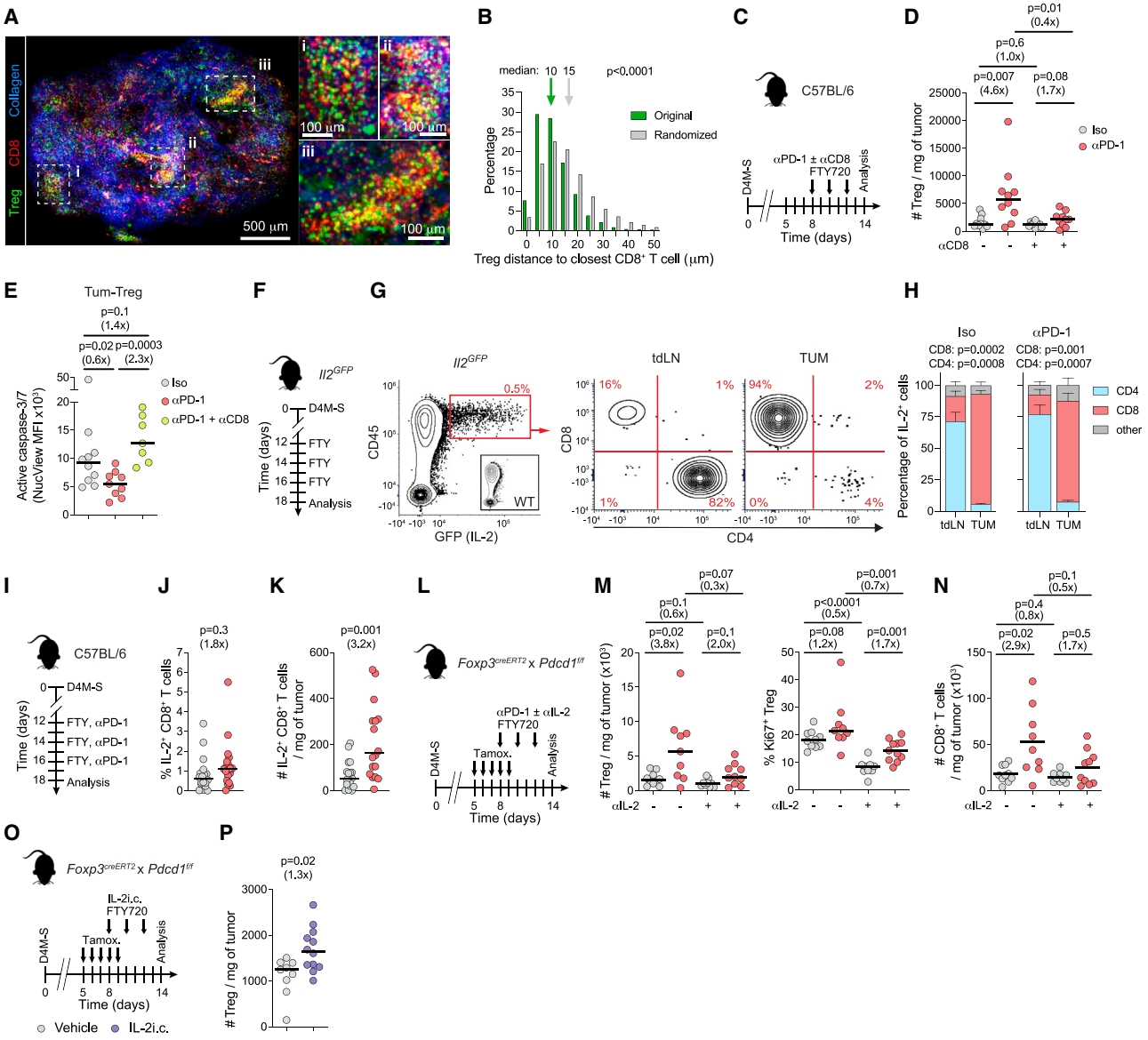

Figure 4. CD8⁺ T cells and IL-2 orchestrate tumor-Treg accumulation after PD-1 blockade

(A) Image of a D4M-S tumor from a *Foxp3*^{GFP}x*E8I*^{cre}x*Rosa26*$^{LSL\text{-}Tomato}$ mouse. Three regions of interest are magnified on the right. One tumor representative of three is shown.

(B) Distribution of Treg distance to the closest CD8⁺ T cell in the original image and after randomization of Treg positions. *p* values by Kolmogorov-Smirnov test.

(C) Scheme for CD8⁺ T cell depletion experiments.

(D) Treg numbers in D4M-S tumor-bearing mice ± αPD-1 and CD8-depleting antibodies.

(E) MFI of NucView (active caspase-3/7) in Tregs from D4M-S melanomas ± αPD-1 and CD8-depleting antibodies. For D and E, n = 7–10 mice/group from 2 independent experiments.

(F) Scheme to determine the source of IL-2.

(G) Dot plot of IL-2-transcribing cells (GFP⁺) in an *Il2*^{GFP} mouse with a wild-type mouse shown in the inset. CD8 and CD4 expression was quantified on GFP⁺ cells.

(H) Proportions of CD4⁺ and CD8⁺ T cells among IL-2 producers in tdLN and D4M-S melanomas treated as indicated. Mean ± SEM of three independent experiments is depicted. *p* values by Student's t test.

(I) Scheme for IL-2 protein quantification ± αPD-1.

(J and K) Percentage (J) and counts (K) of IL-2-producing CD8⁺ T cells ± αPD-1. *n* = 18 mice/group in four experiments.

(L) Scheme for IL-2 neutralization.

(M and N) Treg numbers, Ki67 expression (M), and CD8⁺ T cell counts (N) in D4M-S bearing mice ± αPD-1 and IL-2 neutralization.

(O) Scheme to assess the response of PD-1-deficient tumor-Tregs to IL-2i.c.

(P) Treg numbers within D4M-S tumors ± IL-2i.c. For J–P, *n* = 9–12 mice/group from 2 experiments. In D, E, and J–P bars depict medians and *p* values by Mann-Whitney U test.

See also Figure S4.

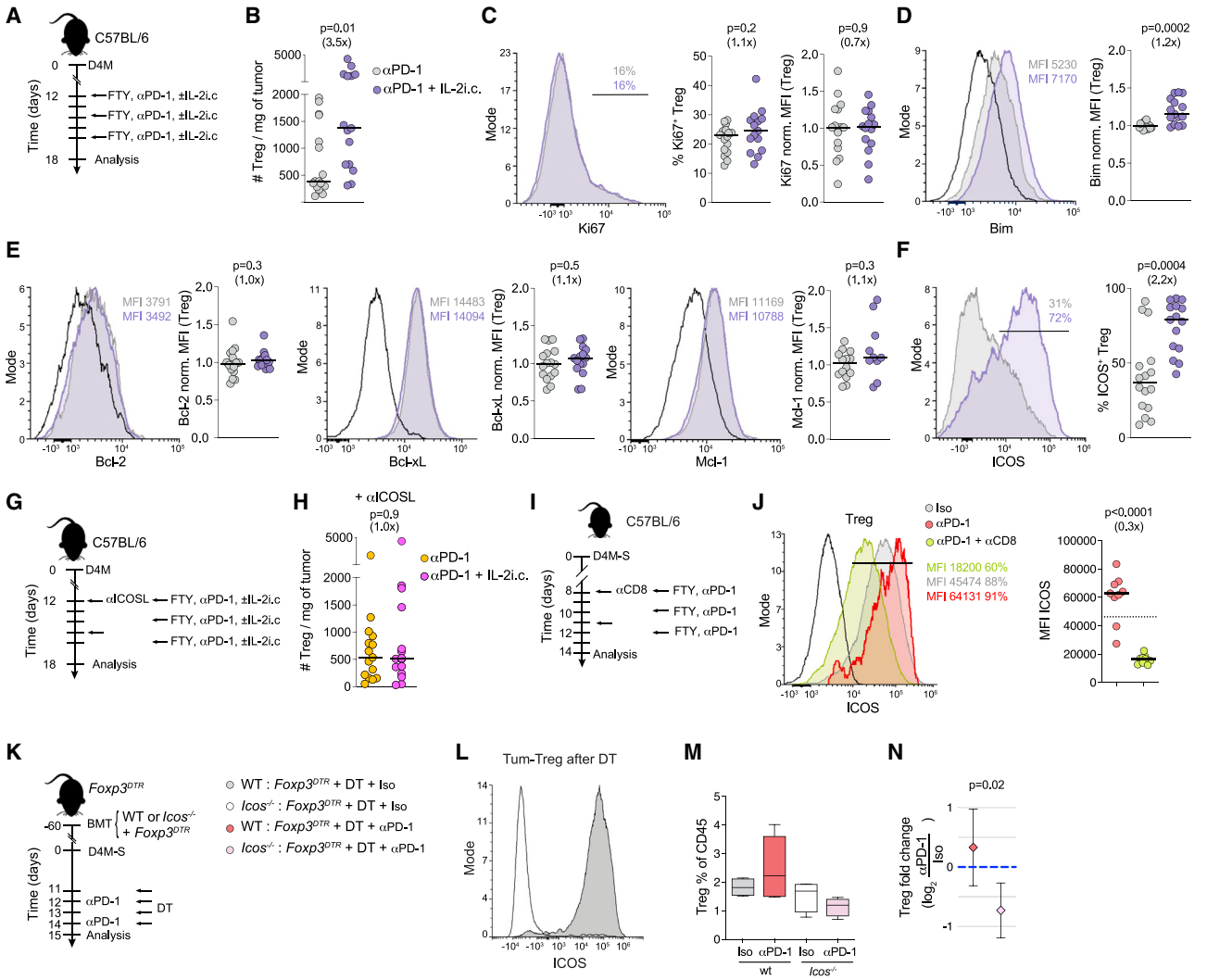

Figure 5. ICOS mediates IL-2-driven tumor-Treg accumulation

(A) Scheme for administration of αPD-1 and IL-2i.c.

(B–F) Numbers (B), Ki67 (C), Bim (D), Bcl-2, Bcl-xL, Mcl-1 (E), and ICOS expression (F) in tumor-Tregs treated with PD-1 blockade ± IL-2i.c.

(G) Scheme for ICOSL blockade.

(H) Tumor-Treg numbers upon treatment with αPD-1 and αICOSL, ± IL-2i.c. For B–H, *n* = 10–16 mice/group from 2 to 3 experiments.

(I) Scheme to quantify ICOS expression after PD-1 blockade and $CD8^+$ T cell depletion.

(J) ICOS expression in tumor-Tregs ± αPD-1 and $CD8^+$ T cell depletion. The dotted line represents the median of the isotype control group. *n* = 8–10 mice/group from 2 independent experiments. For B–J, bars depict medians and *p* values by Mann-Whitney U test.

(K) Scheme for bone marrow chimera experiments evaluating the role of ICOS signaling in tumor-Tregs during PD-1 blockade.

(L) ICOS expression in tumor-Tregs after DT administration.

(M) Tumor-Treg percentage in the indicated groups. Median, interquartile range, and Tukey whiskers are depicted.

(N) Fold change of tumor-Treg percentage after PD-1 blockade, compared to isotype treatment. Separate fold change values were calculated for control and ICOS-deficient Tregs. Mean and standard deviation are depicted, and the *p* value was calculated by Student's t test with Welch correction. *n* = 4–5 mice/group. See also Figure S5.

Tregs (Figure 5K). In these animals, ICOS-deficient Tregs develop together with ICOS-sufficient cells, yet DT administration eliminates the latter, generating an ICOS-deficient Treg compartment (Figure 5L). We used chimeras bearing a 1:1 mix of wild-type and DTR-expressing Tregs as controls. Treatment of D4M-S melanomas with αPD-1 led to increased tumor-Tregs in controls but not in mice bearing ICOS-deficient Tregs (Figures 5M and 5N), indicating that ICOS plays a Treg-intrinsic role in mediating tumor-Treg accumulation after αPD-1. Together, these data demonstrate that the IL-2/ICOS axis orchestrates Treg abundance in melanoma.

Presence of the $CD8^+$ T cell/IL-2/Treg axis in human melanoma

To assess whether the $CD8^+$ T cell/IL-2/Treg axis is also present in human melanomas, we performed CellChat analysis[48] on a

published single-cell RNA sequencing dataset.[13] CellChat uses an annotated receptor-ligand library to calculate the "interaction strength" between all cell clusters in a single-cell RNA sequencing experiment. To eliminate confounding factors represented by the variable treatment of patients, we included only cases treated with αPD-1 monotherapy; the control group comprised all the tumors sampled before treatment. CellChat predicted that PD-1 immunotherapy increases the IL-2/IL2Rαβγ communication pathway between *TCF7*-expressing memory T cells, mostly $CD8^+$ T cells,[13] and Tregs in human melanoma (Figure 6A).

We also used immunofluorescence to assess the colocalization of $CD8^+$ T cells and ICOS-expressing Tregs in human melanoma metastases from one treatment-naïve and two checkpoint blockade immunotherapy-treated patients (Figure S6A). Clusters of $CD8^+$ T cells and Tregs were present in all samples (Figure 6B). These clusters contained ICOS-expressing cells and surrounded tumor cell nests (Figures 6C and S6B). To calculate Treg positions relative to $CD8^+$ T cells, we first applied a nearest-neighbor algorithm to identify $CD8^+$ T cell clusters. We then calculated the distance of each Treg from $CD8^+$ T cell clusters in the original dataset and after randomization of Treg position within the space occupied by immune cells. Randomization increased Treg distance to the nearest $CD8^+$ T cell cluster in all tumors, indicating that Tregs colocalized with $CD8^+$ T cell clusters in the original data (Figure 6D). The αPD-1-treated metastasis was very large and generated data exceeding our available computational power. To overcome this problem, we split the tumor into four zones. Tregs colocalized with $CD8^+$ T cell clusters in all cases (Figures S6C and S6D). We finally observed that ICOS-expressing Tregs localized closer to $CD8^+$ T cell clusters than ICOS-negative Tregs in all tumors (Figures 6E and 6F), suggesting that ICOS expression is induced within clusters. Thus, the $CD8^+$ T cell/IL-2/Treg axis is present in human melanoma.

Concurrent ICOSL/PD-1 blockade does not improve the effectiveness of PD-1 immunotherapy

Because tumor-Tregs expressed the highest levels of ICOS (Figures S7A and S7B), and ICOS prolongs their lifespan, ICOSL inhibition could synergize with PD-1 blockade to increase melanoma rejection. However, ICOS was also expressed at lower levels on Th and $CD8^+$ T cells (Figures S7A and S7B), and its inhibition could decrease anti-tumor functions. To distinguish between these possibilities, we treated C57BL/6 mice bearing immunogenic or non-immunogenic melanomas with concomitant ICOSL/PD-1 blockade in the absence of FTY720, and measured tumor growth (Figures 7A and S7C). The non-immunogenic D4M melanoma was insensitive to individual or combined blockade of PD-1 and ICOSL (Figure S7C). In contrast, αPD-1-treated mice better controlled immunogenic D4M-S tumors than isotype-treated mice. αICOSL alone did not affect D4M-S growth and, when administered in combination with αPD-1, did not improve the efficacy of αPD-1 therapy (Figure 7B). We thus hypothesized that the favorable effects of ICOSL blockade on tumor-Tregs are counterbalanced by a detrimental impact on effector T cells.

Concomitant ICOSL/PD-1 blockade restrains αPD-1-mediated antitumor immunity

We characterized the effects of αICOSL alone or combined with αPD-1 on Treg, $CD8^+$ T cells, and Th cells in the presence of FTY720 to focus on the tumor immune environment (Figure 7C). ICOSL monotherapy decreased Tregs more than Th and $CD8^+$ T cells (Figure 7D), leading to a higher $CD8^+$ T cell/Treg ratio (Figure S7D). PD-1 monotherapy increased the numbers of Treg, $CD8^+$ T cells, and Th cells. However, when ICOSL and PD-1 blockade were combined, the αPD-1-mediated increase in Treg, Th, and $CD8^+$ T cell numbers was negated (Figure 7D). In tumor-associated $CD8^+$ T cells, the expression of granzyme B but not Lamp-1 decreased significantly upon blockade of ICOSL and PD-1 compared to αPD-1 monotherapy. Additionally, there was a tendency toward reduced numbers of IFNγ- and TNF-producing cells. (Figures 7E and S7E). We observed a similar trend in Th cells, even though αPD-1 enhanced their effector functions to a lower level than $CD8^+$ T cells (Figures 7E and S7F). We speculate that the αICOSL/αPD-1 combination had a therapeutic effect similar to the PD-1 monotherapy despite the induced $CD8^+$ T cell dysfunction because Treg numbers were reduced. We also assessed the impact of ICOSL/PD-1 therapy on tumor-associated antigen-presenting cells (APCs) because they express ICOSL.[49] While αPD-1 monotherapy increased the numbers of $XCR1^+$ DC1, $Sirp\alpha^+$ DC2, and tumor-associated macrophages (TAMs), and MHC-I expression compared to isotype controls, the αICOSL/αPD-1 combination negated these effects (Figures S7G and S7H). There was no change in MHC-II, CD80, CD86, and free PD-L1 expression on DC1, DC2, and TAMs during ICOSL/PD-1 blockade compared to PD-1 monotherapy (Figure S7H). Also, αICOSL monotherapy did not change these parameters. These data indicate that while αICOSL alone impairs Tregs with negligible effects on other tumor-associated immune cells, its combination with αPD-1 prevents the enhancement in effector T cell and APC numbers and functions triggered by PD-1 monotherapy.

Sequential ICOSL/PD-1 blockade improves the effectiveness of PD-1 immunotherapy

We explored whether we could leverage the benefits of ICOSL blockade while avoiding its detrimental effects on αPD-1 co-administration. We reasoned that, by first administering αICOSL antibodies to D4M-S bearing mice, we could preferentially decrease tumor-Treg numbers so that subsequent PD-1 blockade would improve the antitumor efficacy of $CD8^+$ T cells (Figure 7F). Compared to PD-1 monotherapy, sequential ICOSL/PD-1 administration decreased Treg numbers (Figure 7G) to a lesser extent than concomitant treatment (Figure 7D) but $CD8^+$ T cell counts were preserved (Figures 7G and 7H) leading to a favorable $CD8^+$ T cell/Treg ratio (Figure S7I). IFNγ and TNF production in $CD8^+$ T cells and Th cells were also maintained (Figures 7H, S7J, and S7K). Sequential ICOSL/PD-1 immunotherapy increased DC1 and DC2 numbers to levels comparable to PD-1 monotherapy, while TAM counts were unchanged (Figures S7L and S7M). Similar to PD-1 monotherapy, sequential treatment promoted class-I and class-II antigen presentation in DC1, DC2, and TAMs (Figure S7M). In line with a previous report,[26] αPD-1 alone or in concomitant or sequential combination with αICOSL decreased CD80 and CD86 expression in DCs. PD-L1 expression increased only in TAMs after PD-1 and concomitant or sequential ICOSL/PD-1 therapy, compared to controls. As clinical tumor immunotherapy does not include FTY720, we characterized the tumor

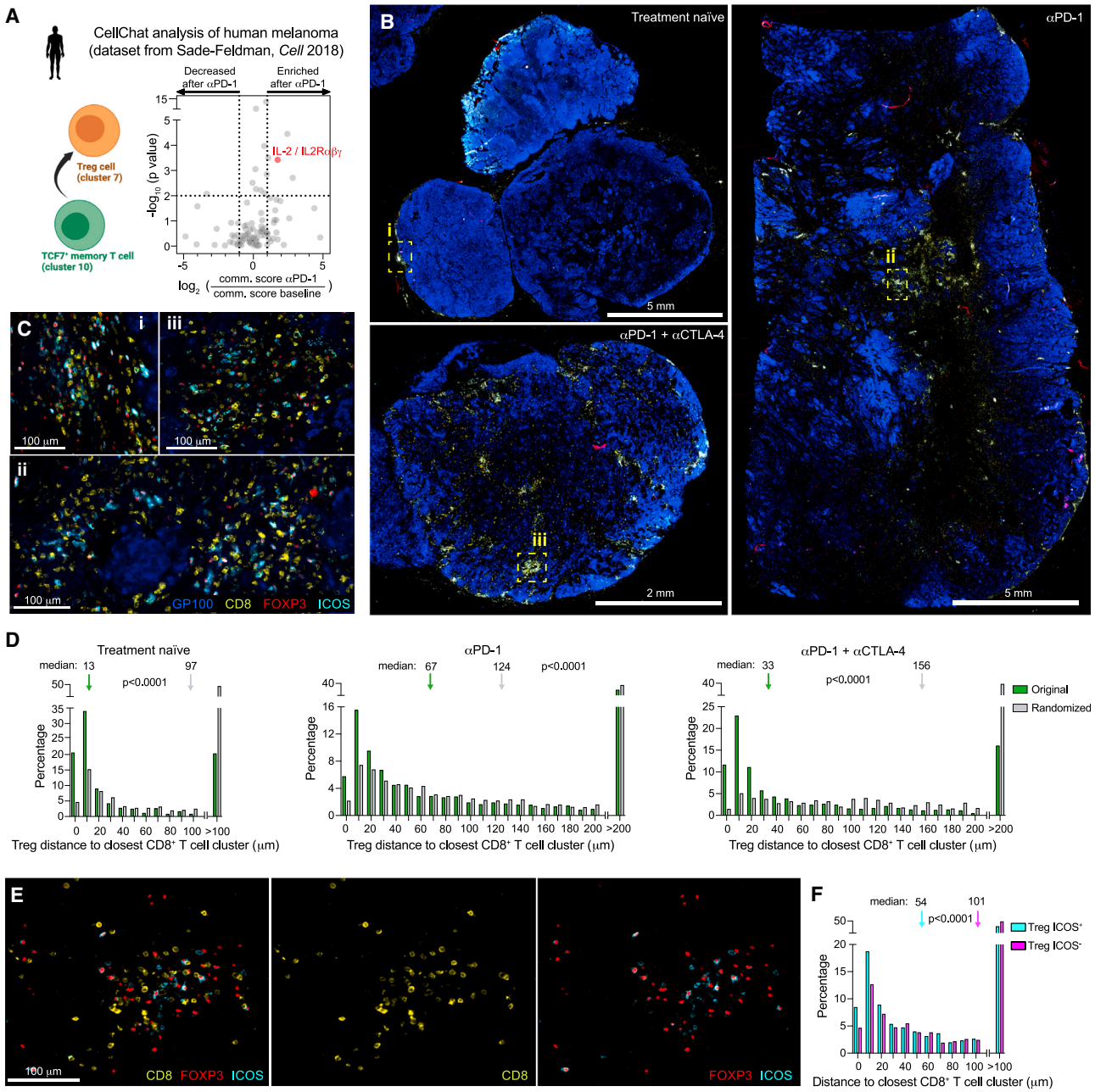

Figure 6. CD8⁺ T cell:Treg crosstalk in human melanomas

(A) CellChat analysis of communication pathways in human melanoma. *TCF7*-expressing memory T cells and Tregs correspond to clusters 10 and 7 of ref.[13] The volcano plot depicts the ratio of communication score after compared to before PD-1 immunotherapy, and the *p* value (Mann-Whitney test) of ligand upregulation following PD-1 blockade. The IL-2/IL2Rαβγ pathway is highlighted in red. All other interactions with a finite log-fold change of communication probability are shown in gray.

(B) Immunofluorescence of human melanoma treated as indicated. Images from all three analyzed patients are shown.

(C) Magnification of Treg and CD8⁺ T cell clusters shown in B.

(D) Distribution of Treg distance to the closest CD8⁺ T cell cluster in the original image and after randomization of Treg positions. The depicted graphs were generated from whole tumors (treatment naive and αPD-1+αCTLA-4) or a representative region (zone 2 for αPD-1, Figures S6C and S6D).

(E) Single- and multi-channel images depicting the distribution of ICOS-expressing Tregs relative to a CD8⁺ T cell cluster.

(F) Quantification of ICOS⁺ and ICOS⁻ Treg distance to the closest CD8⁺ T cell cluster. One representative analysis out of three tumors is shown. *p* values by Kolmogorov-Smirnov test.

See also Figure S6.

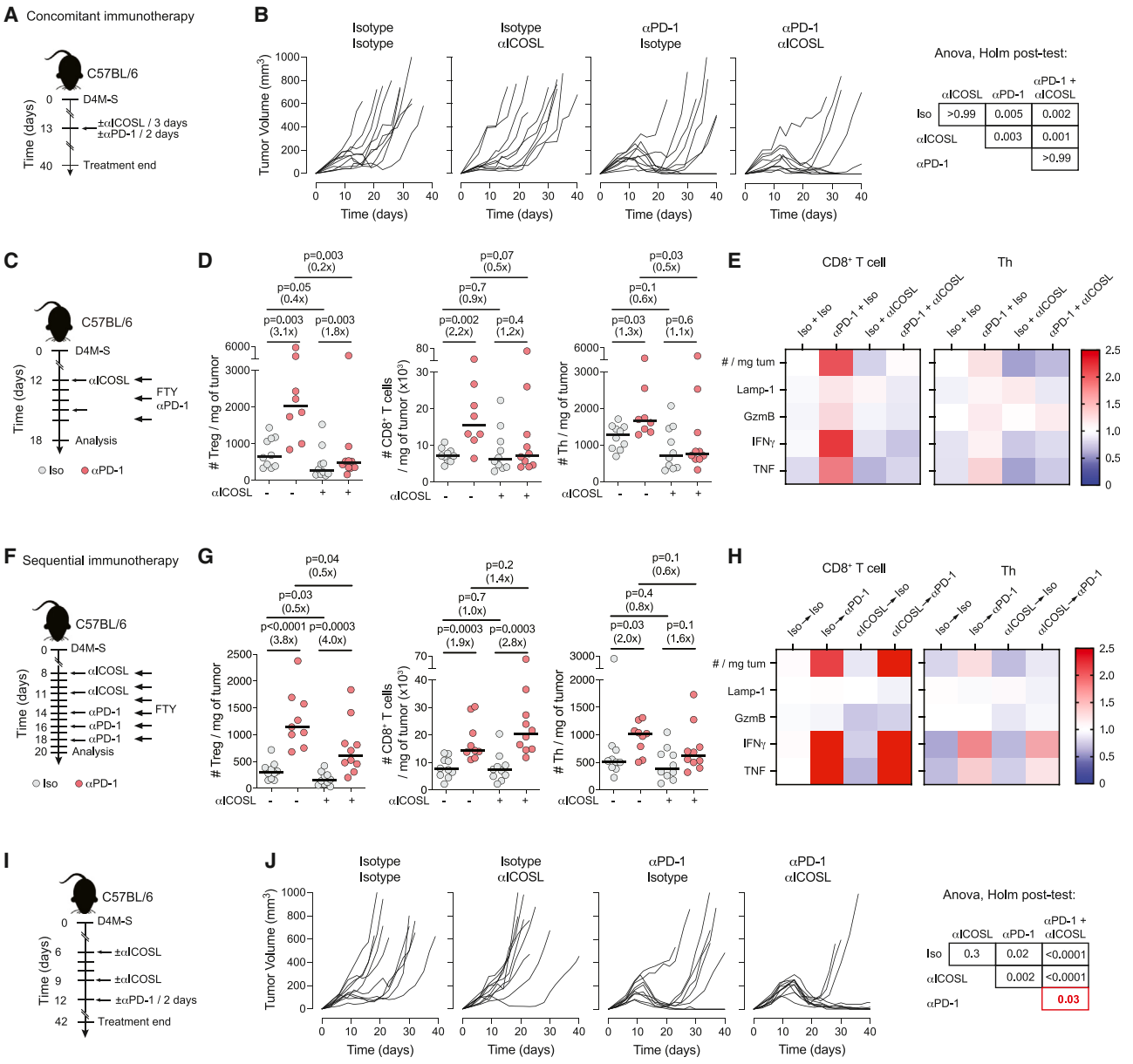

Figure 7. Effectiveness of sequential, but not concomitant, ICOSL/PD-1 immunotherapy

(A) Scheme for concomitant ICOSL/PD-1 therapy.

(B) Growth curves of D4M-S tumors in mice treated with αICOSL or αPD-1 antibodies individually or in combination.

(C) Scheme to characterize the effects of concomitant ICOSL/PD-1 therapy on T cells and APCs.

(D) Treg, CD8$^+$ T cell, and Th cell numbers in D4M-S melanomas treated with αPD-1 or αICOSL antibodies.

(E) Heatmap depicting cell numbers, Lamp-1, granzyme B expression, and number of IFNγ- and TNF-producing cells per mg of tumor after concomitant ICOSL/PD-1 blockade. Colors represent the median of all experimental values, normalized by the average of the isotype/isotype group.

(F) Scheme to investigate the effect of sequential ICOSL/PD-1 blockade on T cells and APCs.

(G and H) T cell counts (G) and heatmap summarizing T cell functions (H) upon sequential αICOSL/αPD-1 immunotherapy. For C–H, n = 8–10 mice/group from 2 experiments. Bars depict medians. *p* values by Mann-Whitney U test.

(I) Scheme for sequential ICOSL/PD-1 immunotherapy.

(J) Growth curves of D4M-S tumors in mice treated with monotherapies or sequential ICOSL/PD-1 immunotherapy. For B and J, each line represents one mouse. *n* = 10 mice/group from 2 separate experiments. *p* values by type II Anova with Holm post-test.

See also Figure S7.

immune environment in its absence. Both sequential and concomitant αICOSL/αPD-1 regimens decreased tumor-Tregs compared to PD-1 monotherapy (Figure S7N). PD-1 monotherapy enhanced Th and CD8$^+$ T cell numbers and cytokine production. Sequential αICOSL/αPD-1 administration performed slightly better than concomitant therapy in preserving CD8$^+$ T cell numbers and function. On the other hand, neither regimen increased Th counts or functions to levels similar to PD-1 monotherapy (Figures S7N–S7R). We also found enhanced DC1 and TAM counts after sequential but not concomitant therapy (Figures S7S and S7T). We did not observe a consistent modulation of APC functionality in any therapeutic regimen (Figure S7T). We posit that in agreement with Figures S1F and S1G, the lymphocyte influx from the circulation limited our ability to detect the immunological consequences of ICOSL/PD-1 immunotherapy within the tumor.

We finally examined the therapeutic outcome of sequential ICOSL/PD-1 blockade without FTY720 (Figure 7I). PD-1 monotherapy resulted in better tumor control than isotype or αICOSL administration (Figure 7J). Importantly, sequential ICOSL/PD-1 blockade significantly improved tumor control over PD-1 monotherapy (Figure 7J), correlating with the decreased Treg responses and preserved CD8$^+$ T cell numbers and function we observed within the tumor environment. Thus, we provide evidence of synergy between sequentially administered ICOSL and PD-1 blockade against immunogenic melanoma.

DISCUSSION

In this study, we found that PD-1 blockade promotes the crosstalk between tumor-associated CD8$^+$ T cells and Tregs, increasing tumor-Treg numbers and reducing the efficacy of immunotherapy against melanoma. We used genetic deletion and F-IVM to demonstrate that interrupting cell-intrinsic PD-1 signaling has a limited impact on TCR-mediated activation and Treg accumulation in tumors. Instead, αPD-1-triggered tumor-Treg increase depended on CD8$^+$ T cells and IL-2 and was mediated by ICOS expression on Tregs. We then targeted ICOS signaling to block the CD8$^+$ T cell:Treg crosstalk and improve the efficacy of PD-1 immunotherapy. Concomitant PD-1 and ICOSL blockade did not enhance the effectiveness of PD-1 monotherapy since αICOSL counteracted the αPD-1-mediated increase of APC and T cell effector functions. However, sequential ICOSL / PD-1 blockade maintained CD8$^+$ T cell numbers and function while decreasing tumor-Treg counts, resulting in improved tumor control compared to PD-1 monotherapy.

A seminal report showed that PD-1 blockade increases the abundance and activation of tumor-associated Tregs in patients with hyper-progressive gastro-esophageal cancer.[14] However, there is no consensus on the effect of PD-1 blockade on melanoma-associated Tregs: one study detected no differences in Treg abundance after treatment,[50] while a subsequent report showed Treg enrichment in the blood of patients not responding to PD-1 immunotherapy.[51] We addressed these discrepancies by performing a meta-analysis on data from patients treated with PD-1 monotherapy only and for whom paired biopsies taken before and on-treatment were available. We found that PD-1 immunotherapy increased the number of tumor-Tregs in most patients. While melanoma is generally immunogenic, variation among individuals is high (1–100 mutations per Mb of exome).[52] Therefore, patients who did not exhibit increased Tregs following αPD-1 treatment may have had a poorly immunogenic cutaneous melanoma or a subtype not caused by ultraviolet exposure (e.g., uveal or mucosal).

A comparison of our current and published data[16] indicates that PD-1 and CTLA-4 blockade impact tumor-Treg activation through different mechanisms. While PD-1 blockade induced the expansion of tumor CD8$^+$ T cells and Tregs and a state of Treg activation characterized by low proliferation and high expression of Foxp3, GITR, and ICOS, CTLA-4 inhibition caused tumor-Treg proliferation and accumulation with no enhancement in activation markers.[16] These differences may be explained by the ability of PD-1 to modulate TCR and CD28 signaling[9,10] while CTLA-4 primarily modulates CD28 signaling,[53] or by the distinct effects of each immunotherapy on the tumor immune environment.[12] In tdLNs, PD-1 blockade increased eTreg percentage and proliferation. The percentage of CD44^{hi}CD62L$^-$CD8$^+$ T cells also increased. These findings agree with a previous study on transgenic mice with T cell-specific PD-1 deficiency.[14] However, we noticed that in response to αPD-1, the characteristics of Treg activation in tdLNs and the tumor environment differed: lymph node Tregs displayed more prominent proliferation but no upregulation of activation markers. The reason for this phenomenon could be that lymph node eTregs must complete several differentiation steps to become Tregs residing in non-lymphoid tissues, including tumors.[54] The notion that the Treg transcriptome changes dynamically during their development fits our observation that PD-1 signaling is critical during the cTreg to eTreg transition in lymph nodes but less so afterward.

Our studies on tumor-Treg activation showed that αPD-1 antibodies only marginally increased TCR signaling, and Treg-specific genetic deletion of PD-1 did not cause their accumulation in immunogenic melanoma. These observations appear to conflict with published reports on pancreatitis,[55] experimental autoimmune encephalomyelitis and type 1 diabetes,[56] *Toxoplasma gondii* infection,[57] and tumors[19] suggesting that PD-1 controls Treg numbers and activation in a cell-intrinsic way. However, the numerical expansion of PD-1-deficient tumor-Tregs after αPD-1 treatment demonstrated that indirect effects of PD-1 immunotherapy dominate over cell-intrinsic PD-1 blockade when controlling Treg numbers in immunogenic tumors. It is unlikely that tumor-Treg accumulation in αPD-1-treated *Foxp3*^{creERT2}x*Pdcd1*$^{f/f}$ mice was due to antibody-mediated PD-1 blockade on the 20% of Tregs that did not delete PD-1. Indeed, even 100% PD-1 inhibition via αPD-1 antibodies did not drive tumor-Treg accumulation without CD8$^+$ T cell support (Figure 4D). Therefore, the relative importance of intrinsic and extrinsic regulation of Treg biology by αPD-1 may depend on the immunological context.

While we cannot exclude that the Treg-intrinsic PD-1 inhibition increases their suppressive function, we demonstrate that Treg number increase, an indirect effect of PD-1 blockade, significantly contributes to tumor growth (Figure 2). While these tumor-Tregs can suppress CD8$^+$ T cell function through many mechanisms, one of them is likely the reduction of CD80 and CD86 expression on DC1 and DC2 via CTLA-4 (Figures S7H,

S7M, and S7T). Both increased tumor-Treg numbers (Figure 1) and CTLA-4 expression per cell ([19] and data not shown) can contribute to CD80 and CD86 modulation after PD-1 blockade. In agreement with this hypothesis, a recent report showed decreased CD80 expression in splenic DC2 after αPD-L1 administration.[26]

One key finding of our study is that CD8$^+$ T cells colocalize with Tregs in tumors and mediate αPD-1-dependent Treg increase. Tumor-associated CD8$^+$ T cells were the dominant source of intratumor IL-2, a surprising finding since Th cells are the primary producers of IL-2 in lymph nodes.[58] Because Th cells are also boosted by PD-1 immunotherapy,[59] the primary source of IL-2 is likely determined by the relative abundance of CD8$^+$ T cells and Th cells within the tumor environment. IL-2 is preferentially secreted at the immunological synapse between effector T cells and APCs[60] but eventually diffuses within tissues.[41,61] Resolution of the immunological synapse is a likely mechanism by which IL-2 is released into the intercellular space; if so, the instability of immune synapses between CD8$^+$ T cells and cancer cells[62] might contribute to IL-2 dissemination within the tumor. We showed that tumor-Tregs interpret IL-2 signaling by upregulating the co-stimulatory and anti-apoptotic molecule ICOS. Previous work defined IL-2 and ICOS as necessary for maintaining cTreg and eTreg homeostasis in secondary lymphoid organs.[25] Our data extend these findings by demonstrating that IL-2 induces ICOS on tumor-Tregs.

We found that αICOSL did not synergize with simultaneous PD-1 immunotherapy because it impacted both Tregs and effector T cells. The observation that CD8$^+$ T cells were the primary source of IL-2, irrespective of PD-1 blockade, opened the possibility that the CD8$^+$ T cell/IL-2/Treg axis could be active before immunotherapy, albeit at lower levels. Therefore, we pre-treated melanoma-bearing mice with αICOSL to reduce Tregs via inhibition of the CD8$^+$ T cell:Treg crosstalk, and subsequently administered PD-1 immunotherapy to boost CD8$^+$ T cell activation. These treatments synergized. Thus, our studies support the emerging concept that immunotherapies targeting Tregs and effector T cells should be administered to condition the immune environment before switching to a second therapeutic intervention enhancing CD8$^+$ T cells.[63] Another possible strategy would be to target ICOS blockade to tumor-Tregs by using bispecific antibodies binding to ICOS and CTLA-4, OX-40, CCR4,[14] or CCR8.[33] In particular, CCR8 is an attractive candidate due to its specific expression on ICOS$^+$ Tregs (our reanalysis of the dataset by Sade-Feldman and coworkers[13]). ICOSL/PD-1 blockade may also be advantageous in settings of neoadjuvant immunotherapy, which is an exciting strategy to treat patients at high risk of developing metastatic disease.[64] Indeed, a recent paper demonstrated that Treg inhibition during neoadjuvant immunotherapy increases the survival of mice bearing metastatic mammary tumors.[65]

Our finding that ICOSL blockade boosts PD-1 immunotherapy contrasts with the current notion that ICOS should be stimulated, rather than blocked, to increase effector T cell functions and promote tumor rejection. However, this concept was developed in the context of CTLA-4 immunotherapy, which specifically induces a population of ICOS-expressing Th cells[12] that are the target for ICOS agonism.[66,67] Therefore, the pattern of ICOS expression induced by distinct immunotherapies may determine whether ICOS signaling should be triggered or blocked to improve antitumor efficacy.

Human αICOSL antibodies are in clinical development to treat autoimmune diseases,[68,69] and they may be repurposed to treat immunogenic cancers in asynchronous combination with αPD-1. ICOSL blockade offers a better safety profile than ICOS-depleting antibodies, which may eliminate ICOS-expressing Tregs in tumors and other non-lymphoid tissues, increasing the risk of autoimmunity. Since some patients treated with PD-1 monotherapy develop life-threatening immune-related adverse events,[70] increasing the efficacy of immunotherapy avoiding Treg depletion is paramount. The concept of interrupting CD8$^+$ T cell-mediated support to Tregs within the tumor environment might aid in achieving this goal.

Limitations of the study

Our study focused on the mechanisms of tumor-Treg accumulation after PD-1 blockade but did not analyze Treg suppressive function in detail. Nonetheless, our finding that PD-1 blockade moderately enhances TCR signaling in Tregs is compatible with the previously reported increased suppressive function.[19] In addition, our data indicate an important role for IL-2 secretion from CD8$^+$ T cells in supporting tumor-Treg accumulation. However, we did not exclude Th cells as another possible source of IL-2. Finally, the present work shows that inhibition of CD8$^+$ T cell:Treg crosstalk using αICOSL antibodies can improve the outcome of PD-1 immunotherapy. Essential questions regarding the direct comparison between concomitant and sequential schedules, and optimization of the frequency of αICOSL relative to αPD-1 administration will be the focus of future translational studies.

STAR★METHODS

Detailed methods are provided in the online version of this paper and include the following:

- KEY RESOURCES TABLE
- RESOURCE AVAILABILITY
  - Lead contact
  - Materials availability
  - Data and code availability
- EXPERIMENTAL MODEL AND STUDY PARTICIPANT DETAILS
  - Cells
  - Mice
  - Melanoma specimens
- METHOD DETAILS
  - Analysis of existing human datasets
  - Antibody treatment of tumor-bearing mice
  - Measurement of immunotherapy-treated tumors
  - Diphtheria toxin treatment
  - Bone marrow chimeras
  - Flow cytometry
  - Phospho-flow
  - Preparation of mice for F-IVM studies
  - F-IVM time-lapse recordings
  - Analysis of cell motility and Salsa6f signaling
  - Analysis of CD8$^+$ T cell:Treg colocalization in mouse and human melanomas
- QUANTIFICATION AND STATISTICAL ANALYSIS

SUPPLEMENTAL INFORMATION

Supplemental information can be found online at https://doi.org/10.1016/j.ccell.2024.05.013.

ACKNOWLEDGMENTS

This work is funded by pilot grants from the Chao Family Comprehensive Cancer Center (CFCCC) and the Cancer Systems Biology Center of the University of California Irvine, the Melanoma Research Alliance grant #929155, and the DoD Team grant ME220176P1 (F.M.); NSF grant DMS1763272 and grant 594598 from the Simons Foundation (Q.N.); and NIH grants R01AI168063 and U01AI160397 (S.O.). S.N.G. is supported by T32 AI177324; A.M. by T32 AR080622 and NIH-NIAMS F31 AR083279; and R.S.S. by a diversity supplement (primary grant NS120060 PI Villalta) and an NSF-GRFP fellowship. D.S.B.H. acknowledges support from the Adelson Foundation. We thank Drs. Timothy Buschman (Princeton Neuroscience Institute) and Sarah Henrickson (Children's Hospital Philadelphia) for the original Matlab code. We also thank Dr. Jennifer Wargo (MD Anderson Cancer Center) for sharing a bulk RNA sequencing dataset.[29] The authors wish to acknowledge the support of the CFCCC Transgenic Mouse Facility Shared Resource, supported by the NIH-NCI under award number P30CA062203. The graphical abstract is licensed by Biorender.

AUTHOR CONTRIBUTIONS

S.N.G. performed experiments, analyzed data, and wrote the paper; A.M., C.M., and R.S. performed experiments; R.S.S., B.L.W., and Q.N. analyzed human data; M.A.B., D.S.B.H., and A.K.G. provided patient samples; S.N.H. and C.T.W. provided reagents; G.G. and M.H. analyzed F-IVM experiments; T.R.M. provided MC38 tumor data; S.O. conducted F-IVM experiments and supervised movie analysis; F.M. conceived the project, performed experiments, analyzed data, and wrote the paper.

DECLARATION OF INTERESTS

T.R.M. is a founder and shareholder in Monopteros Therapeutics, Inc. This commercial relationship is unrelated to this study.

Received: May 16, 2023
Revised: February 28, 2024
Accepted: May 14, 2024
Published: June 10, 2024

REFERENCES

1. Borghaei, H., Paz-Ares, L., Horn, L., Spigel, D.R., Steins, M., Ready, N.E., Chow, L.Q., Vokes, E.E., Felip, E., Holgado, E., et al. (2015). Nivolumab versus docetaxel in advanced nonsquamous non-small-cell lung cancer. N. Engl. J. Med. *373*, 1627–1639.
2. Ferris, R.L., Blumenschein, G., Fayette, J., Guigay, J., Colevas, A.D., Licitra, L., Harrington, K., Kasper, S., Vokes, E.E., Even, C., et al. (2016). Nivolumab for recurrent squamous-cell carcinoma of the head and neck. N. Engl. J. Med. *375*, 1856–1867.
3. Nghiem, P.T., Bhatia, S., Lipson, E.J., Kudchadkar, R.R., Miller, N.J., Annamalai, L., Berry, S., Chartash, E.K., Daud, A., Fling, S.P., et al. (2016). PD-1 blockade with pembrolizumab in advanced merkel-cell carcinoma. N. Engl. J. Med. *374*, 2542–2552.
4. Migden, M.R., Rischin, D., Schmults, C.D., Guminski, A., Hauschild, A., Lewis, K.D., Chung, C.H., Hernandez-Aya, L., Lim, A.M., Chang, A.L.S., et al. (2018). PD-1 Blockade with Cemiplimab in Advanced Cutaneous Squamous-Cell Carcinoma. N. Engl. J. Med. *379*, 341–351.
5. Motzer, R.J., Tannir, N.M., McDermott, D.F., Arén Frontera, O., Melichar, B., Choueiri, T.K., Plimack, E.R., Barthélémy, P., Porta, C., George, S., et al. (2018). Nivolumab plus Ipilimumab versus Sunitinib in advanced renal-cell carcinoma. N. Engl. J. Med. *378*, 1277–1290.
6. Larkin, J., Chiarion-Sileni, V., Gonzalez, R., Grob, J.-J., Rutkowski, P., Lao, C.D., Cowey, C.L., Schadendorf, D., Wagstaff, J., Dummer, R., et al. (2019). Five-Year Survival with Combined Nivolumab and Ipilimumab in Advanced Melanoma. N. Engl. J. Med. *381*, 1535–1546.
7. André, T., Shiu, K.-K., Kim, T.W., Jensen, B.V., Jensen, L.H., Punt, C., Smith, D., Garcia-Carbonero, R., Benavides, M., Gibbs, P., et al. (2020). Pembrolizumab in Microsatellite-Instability–High Advanced Colorectal Cancer. N. Engl. J. Med. *383*, 2207–2218.
8. Sharma, P., Hu-Lieskovan, S., Wargo, J.A., and Ribas, A. (2017). Primary, Adaptive, and Acquired Resistance to Cancer Immunotherapy. Cell *168*, 707–723.
9. Yokosuka, T., Takamatsu, M., Kobayashi-Imanishi, W., Hashimoto-Tane, A., Azuma, M., and Saito, T. (2012). Programmed cell death 1 forms negative costimulatory microclusters that directly inhibit T cell receptor signaling by recruiting phosphatase SHP2. J. Exp. Med. *209*, 1201–1217.
10. Hui, E., Cheung, J., Zhu, J., Su, X., Taylor, M.J., Wallweber, H.A., Sasmal, D.K., Huang, J., Kim, J.M., Mellman, I., and Vale, R.D. (2017). T cell costimulatory receptor CD28 is a primary target for PD-1-mediated inhibition. Science *355*, 1428–1433.
11. Tumeh, P.C., Harview, C.L., Yearley, J.H., Shintaku, I.P., Taylor, E.J.M., Robert, L., Chmielowski, B., Spasic, M., Henry, G., Ciobanu, V., et al. (2014). PD-1 blockade induces responses by inhibiting adaptive immune resistance. Nature *515*, 568–571.
12. Wei, S.C., Levine, J.H., Cogdill, A.P., Zhao, Y., Anang, N.A.A.S., Andrews, M.C., Sharma, P., Wang, J., Wargo, J.A., Pe'er, D., and Allison, J.P. (2017). Distinct Cellular Mechanisms Underlie Anti-CTLA-4 and Anti-PD-1 Checkpoint Blockade. Cell *170*, 1120–1133.e17.
13. Sade-Feldman, M., Yizhak, K., Bjorgaard, S.L., Ray, J.P., de Boer, C.G., Jenkins, R.W., Lieb, D.J., Chen, J.H., Frederick, D.T., Barzily-Rokni, M., et al. (2018). Defining T Cell States Associated with Response to Checkpoint Immunotherapy in Melanoma. Cell *175*, 998–1013.e20.
14. Kamada, T., Togashi, Y., Tay, C., Ha, D., Sasaki, A., Nakamura, Y., Sato, E., Fukuoka, S., Tada, Y., Tanaka, A., et al. (2019). PD-1+ regulatory T cells amplified by PD-1 blockade promote hyperprogression of cancer. Proc. Natl. Acad. Sci. USA *116*, 9999–10008.
15. Marangoni, F., Zhang, R., Mani, V., Thelen, M., Ali Akbar, N.J., Warner, R.D., Äijö, T., Zappulli, V., Martinez, G.J., Turka, L.A., and Mempel, T.R. (2018). Tumor Tolerance–Promoting Function of Regulatory T Cells Is Optimized by CD28, but Strictly Dependent on Calcineurin. J. Immunol. *200*, 3647–3661.
16. Marangoni, F., Zhakyp, A., Corsini, M., Geels, S.N., Carrizosa, E., Thelen, M., Mani, V., Prüßmann, J.N., Warner, R.D., Ozga, A.J., et al. (2021). Expansion of tumor-associated Treg cells upon disruption of a CTLA-4-dependent feedback loop. Cell *184*, 3998–4015.e19.
17. Bauer, C.A., Kim, E.Y., Marangoni, F., Carrizosa, E., Claudio, N.M., and Mempel, T.R. (2014). Dynamic Treg interactions with intratumoral APCs promote local CTL dysfunction. J. Clin. Invest. *124*, 2425–2440.
18. Shang, B., Liu, Y., Jiang, S.J., and Liu, Y. (2015). Prognostic value of tumor-infiltrating FoxP3+ regulatory T cells in cancers: A systematic review and meta-analysis. Sci. Rep. *5*, 15179.
19. Kumagai, S., Togashi, Y., Kamada, T., Sugiyama, E., Nishinakamura, H., Takeuchi, Y., Vitaly, K., Itahashi, K., Maeda, Y., Matsui, S., et al. (2020). The PD-1 expression balance between effector and regulatory T cells predicts the clinical efficacy of PD-1 blockade therapies. Nat. Immunol. *21*, 1346–1358.
20. Jenkins, M.H., Steinberg, S.M., Alexander, M.P., Fisher, J.L., Ernstoff, M.S., Turk, M.J., Mullins, D.W., and Brinckerhoff, C.E. (2014). Multiple murine BRafV600E melanoma cell lines with sensitivity to PLX4032. Pigment Cell Melanoma Res. *27*, 495–501.
21. Di Pilato, M., Kim, E.Y., Cadilha, B.L., Prüßmann, J.N., Nasrallah, M.N., Seruggia, D., Usmani, S.M., Misale, S., Zappulli, V., Carrizosa, E., et al. (2019). Targeting the CBM complex causes Treg cells to prime tumours for immune checkpoint therapy. Nature *570*, 112–116.

22. Matloubian, M., Lo, C.G., Cinamon, G., Lesneski, M.J., Xu, Y., Brinkmann, V., Allende, M.L., Proia, R.L., and Cyster, J.G. (2004). Lymphocyte egress from thymus and peripheral lymphoid organs is dependent on S1P receptor 1. Nature *427*, 355–360.

23. Mandala, S., Hajdu, R., Bergstrom, J., Quackenbush, E., Xie, J., Milligan, J., Thornton, R., Shei, G.J., Card, D., Keohane, C., et al. (2002). Alteration of lymphocyte trafficking by sphingosine-1-phosphate receptor agonists. Science *296*, 346–349.

24. Lo, J.A., Kawakubo, M., Juneja, V.R., Su, M.Y., Erlich, T.H., LaFleur, M.W., Kemeny, L.V., Rashid, M., Malehmir, M., Rabi, S.A., et al. (2021). Epitope spreading toward wild-type melanocyte-lineage antigens rescues suboptimal immune checkpoint blockade responses. Sci. Transl. Med. *13*, eabd8636.

25. Smigiel, K.S., Richards, E., Srivastava, S., Thomas, K.R., Dudda, J.C., Klonowski, K.D., and Campbell, D.J. (2014). CCR7 provides localized access to IL-2 and defines homeostatically distinct regulatory T cell subsets. J. Exp. Med. *211*, 121–136.

26. Pereira, J.A., Lanzar, Z., Clark, J.T., Hart, A.P., Douglas, B.B., Shallberg, L., O'Dea, K., Christian, D.A., and Hunter, C.A. (2023). PD-1 and CTLA-4 exert additive control of effector regulatory T cells at homeostasis. Front. Immunol. *14*, 997376.

27. Riaz, N., Havel, J.J., Makarov, V., Desrichard, A., Urba, W.J., Sims, J.S., Hodi, F.S., Martín-Algarra, S., Mandal, R., Sharfman, W.H., et al. (2017). Tumor and Microenvironment Evolution during Immunotherapy with Nivolumab. Cell *171*, 934–949.e16.

28. Gide, T.N., Quek, C., Menzies, A.M., Tasker, A.T., Shang, P., Holst, J., Madore, J., Lim, S.Y., Velickovic, R., Wongchenko, M., et al. (2019). Distinct Immune Cell Populations Define Response to Anti-PD-1 Monotherapy and Anti-PD-1/Anti-CTLA-4 Combined Therapy. Cancer Cell *35*, 238–255.e6.

29. Helmink, B.A., Reddy, S.M., Gao, J., Zhang, S., Basar, R., Thakur, R., Yizhak, K., Sade-Feldman, M., Blando, J., Han, G., et al. (2020). B cells and tertiary lymphoid structures promote immunotherapy response. Nature *577*, 549–555.

30. Huang, A.C., Orlowski, R.J., Xu, X., Mick, R., George, S.M., Yan, P.K., Manne, S., Kraya, A.A., Wubbenhorst, B., Dorfman, L., et al. (2019). A single dose of neoadjuvant PD-1 blockade predicts clinical outcomes in resectable melanoma. Nat. Med. *25*, 454–461.

31. Arce Vargas, F., Furness, A.J.S., Solomon, I., Joshi, K., Mekkaoui, L., Lesko, M.H., Miranda Rota, E., Dahan, R., Georgiou, A., Sledzinska, A., et al. (2017). Fc-Optimized Anti-CD25 Depletes Tumor-Infiltrating Regulatory T Cells and Synergizes with PD-1 Blockade to Eradicate Established Tumors. Immunity *46*, 577–586.

32. Dodagatta-Marri, E., Meyer, D.S., Reeves, M.Q., Paniagua, R., To, M.D., Binnewies, M., Broz, M.L., Mori, H., Wu, D., Adoumie, M., et al. (2019). α-PD-1 therapy elevates Treg/Th balance and increases tumor cell pSmad3 that are both targeted by α-TGFβ antibody to promote durable rejection and immunity in squamous cell carcinomas. J. Immunother. Cancer *7*, 62.

33. Kidani, Y., Nogami, W., Yasumizu, Y., Kawashima, A., Tanaka, A., Sonoda, Y., Tona, Y., Nashiki, K., Matsumoto, R., Hagiwara, M., et al. (2022). CCR8-targeted specific depletion of clonally expanded Treg cells in tumor tissues evokes potent tumor immunity with long-lasting memory. Proc. Natl. Acad. Sci. USA *119*, e2114282119.

34. Dong, T.X., Othy, S., Jairaman, A., Skupsky, J., Zavala, A., Parker, I., Dynes, J.L., and Cahalan, M.D. (2017). T-cell calcium dynamics visualized in a ratiometric tdTomato-GCaMP6f transgenic reporter mouse. Elife *6*, e32417.

35. Chinen, T., Kannan, A.K., Levine, A.G., Fan, X., Klein, U., Zheng, Y., Gasteiger, G., Feng, Y., Fontenot, J.D., and Rudensky, A.Y. (2016). An essential role for the IL-2 receptor in T reg cell function. Nat. Immunol. *17*, 1322–1333.

36. Owen, D.L., Mahmud, S.A., Vang, K.B., Kelly, R.M., Blazar, B.R., Smith, K.A., and Farrar, M.A. (2018). Identification of Cellular Sources of IL-2 Needed for Regulatory T Cell Development and Homeostasis. J. Immunol. *200*, 3926–3933.

37. Kahan, S.M., Bakshi, R.K., Ingram, J.T., Hendrickson, R.C., Lefkowitz, E.J., Crossman, D.K., Harrington, L.E., Weaver, C.T., and Zajac, A.J. (2022). Intrinsic IL-2 production by effector CD8 T cells affects IL-2 signaling and promotes fate decisions, stemness, and protection. Sci. Immunol. *7*, eabl6322.

38. Siddiqui, I., Schaeuble, K., Chennupati, V., Fuertes Marraco, S.A., Calderon-Copete, S., Pais Ferreira, D., Carmona, S.J., Scarpellino, L., Gfeller, D., Pradervand, S., et al. (2019). Intratumoral Tcf1 + PD-1 + CD8 + T Cells with Stem-like Properties Promote Tumor Control in Response to Vaccination and Checkpoint Blockade Immunotherapy. Immunity *50*, 195–211.e10.

39. DiToro, D., Winstead, C.J., Pham, D., Witte, S., Andargachew, R., Singer, J.R., Wilson, C.G., Zindl, C.L., Luther, R.J., Silberger, D.J., et al. (2018). Differential IL-2 expression defines developmental fates of follicular versus nonfollicular helper T cells. Science *361*, eaao2933.

40. Pierson, W., Cauwe, B., Policheni, A., Schlenner, S.M., Franckaert, D., Berges, J., Humblet-Baron, S., Schönefeldt, S., Herold, M.J., Hildeman, D., et al. (2013). Antiapoptotic Mcl-1 is critical for the survival and niche-filling capacity of Foxp3+ regulatory T cells. Nat. Immunol. *14*, 959–965.

41. Liu, Z., Gerner, M.Y., Van Panhuys, N., Levine, A.G., Rudensky, A.Y., and Germain, R.N. (2015). Immune homeostasis enforced by co-localized effector and regulatory T cells. Nature *528*, 225–230.

42. Boyman, O., Kovar, M., Rubinstein, M.P., Surh, C.D., and Sprent, J. (2006). Selective stimulation of T cell subsets with antibody-cytokine immune complexes. Science *311*, 1924–1927.

43. Li, Q., Shakya, A., Guo, X., Zhang, H., Tantin, D., Jensen, P.E., and Chen, X. (2012). Constitutive Nuclear Localization of NFAT in Foxp3 + Regulatory T Cells Independent of Calcineurin Activity. J. Immunol. *188*, 4268–4277.

44. He, X., Smeets, R.L., Van Rijssen, E., Boots, A.M.H., Joosten, I., and Koenen, H.J.P.M. (2017). Single CD28 stimulation induces stable and polyclonal expansion of human regulatory T cells. Sci. Rep. *7*, 43003–43011.

45. Mittelsteadt, K.L., Hayes, E.T., and Campbell, D.J. (2021). ICOS signaling limits regulatory T cell accumulation and function in visceral adipose tissue. J. Exp. Med. *218*, e20201142.

46. Burmeister, Y., Lischke, T., Dahler, A.C., Mages, H.W., Lam, K.-P., Coyle, A.J., Kroczek, R.A., and Hutloff, A. (2008). ICOS Controls the Pool Size of Effector-Memory and Regulatory T Cells. J. Immunol. *180*, 774–782.

47. Redpath, S.A., van der Werf, N., Cervera, A.M., Macdonald, A.S., Gray, D., Maizels, R.M., and Taylor, M.D. (2013). ICOS controls Foxp3+ regulatory T-cell expansion, maintenance and IL-10 production during helminth infection. Eur. J. Immunol. *43*, 705–715.

48. Jin, S., Guerrero-Juarez, C.F., Zhang, L., Chang, I., Ramos, R., Kuan, C.H., Myung, P., Plikus, M.V., and Nie, Q. (2021). Inference and analysis of cell-cell communication using CellChat. Nat. Commun. *12*, 1088–1120.

49. Aicher, A., Hayden-Ledbetter, M., Brady, W.A., Pezzutto, A., Richter, G., Magaletti, D., Buckwalter, S., Ledbetter, J.A., and Clark, E.A. (2000). Characterization of Human Inducible Costimulator Ligand Expression and Function. J. Immunol. *164*, 4689–4696.

50. Ribas, A., Shin, D.S., Zaretsky, J., Frederiksen, J., Cornish, A., Avramis, E., Seja, E., Kivork, C., Siebert, J., Kaplan-Lefko, P., et al. (2016). PD-1 blockade expands intratumoral memory T cells. Cancer Immunol. Res. *4*, 194–203.

51. Woods, D.M., Ramakrishnan, R., Laino, A.S., Berglund, A., Walton, K., Betts, B.C., and Weber, J.S. (2018). Decreased suppression and increased phosphorylated STAT3 in regulatory T cells are associated

with benefit from adjuvant PD-1 blockade in resected metastatic melanoma. Clin. Cancer Res. *24*, 6236–6247.

52. Lawrence, M.S., Stojanov, P., Polak, P., Kryukov, G.V., Cibulskis, K., Sivachenko, A., Carter, S.L., Stewart, C., Mermel, C.H., Roberts, S.A., et al. (2013). Mutational heterogeneity in cancer and the search for new cancer-associated genes. Nature *499*, 214–218.
53. Qureshi, O.S., Zheng, Y., Nakamura, K., Attridge, K., Manzotti, C., Schmidt, E.M., Baker, J., Jeffery, L.E., Kaur, S., Briggs, Z., et al. (2011). Trans-endocytosis of CD80 and CD86: A molecular basis for the cell-extrinsic function of CTLA-4. Science *332*, 600–603.
54. Miragaia, R.J., Gomes, T., Chomka, A., Jardine, L., Riedel, A., Hegazy, A.N., Whibley, N., Tucci, A., Chen, X., Lindeman, I., et al. (2019). Single-Cell Transcriptomics of Regulatory T Cells Reveals Trajectories of Tissue Adaptation. Immunity *50*, 493–504.e7.
55. Zhang, B., Chikuma, S., Hori, S., Fagarasan, S., and Honjo, T. (2016). Nonoverlapping roles of PD-1 and FoxP3 in maintaining immune tolerance in a novel autoimmune pancreatitis mouse model. Proc. Natl. Acad. Sci. USA *113*, 8490–8495.
56. Tan, C.L., Kuchroo, J.R., Sage, P.T., Liang, D., Francisco, L.M., Buck, J., Thaker, Y.R., Zhang, Q., McArdel, S.L., Juneja, V.R., et al. (2021). PD-1 restraint of regulatory T cell suppressive activity is critical for immune tolerance. J. Exp. Med. *218*, e20182232.
57. Perry, J.A., Shallberg, L., Clark, J.T., Gullicksrud, J.A., DeLong, J.H., Douglas, B.B., Hart, A.P., Lanzar, Z., O'Dea, K., Konradt, C., et al. (2022). PD-L1–PD-1 interactions limit effector regulatory T cell populations at homeostasis and during infection. Nat. Immunol. *23*, 743–756.
58. Boyman, O., and Sprent, J. (2012). The role of interleukin-2 during homeostasis and activation of the immune system. Nat. Rev. Immunol. *12*, 180–190.
59. Nagasaki, J., Togashi, Y., Sugawara, T., Itami, M., Yamauchi, N., Yuda, J., Sugano, M., Ohara, Y., Minami, Y., Nakamae, H., et al. (2020). The critical role of CD41 T cells in PD-1 blockade against MHC-II–expressing tumors such as classic Hodgkin lymphoma. Blood Adv. *4*, 4069–4082.
60. Huse, M., Lillemeier, B.F., Kuhns, M.S., Chen, D.S., and Davis, M.M. (2006). T cells use two directionally distinct pathways for cytokine secretion. Nat. Immunol. *7*, 247–255.
61. Oyler-Yaniv, A., Oyler-Yaniv, J., Whitlock, B.M., Liu, Z., Germain, R.N., Huse, M., Altan-Bonnet, G., and Krichevsky, O. (2017). A Tunable Diffusion-Consumption Mechanism of Cytokine Propagation Enables Plasticity in Cell-to-Cell Communication in the Immune System. Immunity *46*, 609–620.
62. Marangoni, F., Murooka, T.T., Manzo, T., Kim, E.Y., Carrizosa, E., Elpek, N.M., and Mempel, T.R. (2013). The Transcription Factor NFAT Exhibits Signal Memory during Serial T Cell Interactions with Antigen-Presenting Cells. Immunity *38*, 237–249.
63. Ha, D., Tanaka, A., Kibayashi, T., Tanemura, A., Sugiyama, D., Wing, J.B., Lim, E.L., Teng, K.W.W., Adeegbe, D., Newell, E.W., et al. (2019). Differential control of human Treg and effector T cells in tumor immunity by Fc-engineered anti–CTLA-4 antibody. Proc. Natl. Acad. Sci. USA *116*, 609–618.
64. Patel, S.P., Othus, M., Chen, Y., Wright, G.P., Jr., Yost, K.J., Hyngstrom, J.R., Hu-Lieskovan, S., Lao, C.D., Fecher, L.A., Truong, T.G., et al. (2023). Neoadjuvant–Adjuvant or Adjuvant-Only Pembrolizumab in Advanced Melanoma. N. Engl. J. Med. *388*, 813–823.
65. Blomberg, O.S., Kos, K., Spagnuolo, L., Isaeva, O.I., Garner, H., Wellenstein, M.D., Bakker, N., Duits, D.E.M., Kersten, K., Klarenbeek, S., et al. (2023). Neoadjuvant immune checkpoint blockade triggers persistent and systemic Treg activation which blunts therapeutic efficacy against metastatic spread of breast tumors. OncoImmunology *12*, 2201147.
66. Fu, T., He, Q., and Sharma, P. (2011). The ICOS/ICOSL pathway is required for optimal antitumor responses mediated by anti-CTLA-4 therapy. Cancer Res. *71*, 5445–5454.
67. Chen, H., Fu, T., Suh, W.K., Tsavachidou, D., Wen, S., Gao, J., Ng Tang, D., He, Q., Sun, J., and Sharma, P. (2014). CD4 T cells require ICOS-mediated PI3K signaling to increase T-Bet expression in the setting of anti-CTLA-4 therapy. Cancer Immunol. Res. *2*, 167–176.
68. Cheng, L.E., Amoura, Z., Cheah, B., Hiepe, F., Sullivan, B.A., Zhou, L., Arnold, G.E., Tsuji, W.H., Merrill, J.T., and Chung, J.B. (2018). Brief Report: A Randomized, Double-Blind, Parallel-Group, Placebo-Controlled, Multiple-Dose Study to Evaluate AMG 557 in Patients With Systemic Lupus Erythematosus and Active Lupus Arthritis. Arthritis Rheumatol. *70*, 1071–1076.
69. Sullivan, B.A., Tsuji, W., Kivitz, A., Peng, J., Arnold, G.E., Boedigheimer, M.J., Chiu, K., Green, C.L., Kaliyaperumal, A., Wang, C., et al. (2016). Inducible T-cell co-stimulator ligand (ICOSL) blockade leads to selective inhibition of anti-KLH IgG responses in subjects with systemic lupus erythematosus. Lupus Sci. Med. *3*, e000146.
70. Wang, D.Y., Salem, J.E., Cohen, J.V., Chandra, S., Menzer, C., Ye, F., Zhao, S., Das, S., Beckermann, K.E., Ha, L., et al. (2018). Fatal Toxic Effects Associated With Immune Checkpoint Inhibitors: A Systematic Review and Meta-analysis. JAMA Oncol. *4*, 1721–1728.
71. Maekawa, Y., Minato, Y., Ishifune, C., Kurihara, T., Kitamura, A., Kojima, H., Yagita, H., Sakata-Yanagimoto, M., Saito, T., Taniuchi, I., et al. (2008). Notch2 integrates signaling by the transcription factors RBP-J and CREB1 to promote T cell cytotoxicity. Nat. Immunol. *9*, 1140–1147.
72. Rubtsov, Y.P., Niec, R.E., Josefowicz, S., Li, L., Darce, J., Mathis, D., Benoist, C., and Rudensky, A.Y. (2010). Stability of the regulatory T cell lineage *in vivo*. Science *329*, 1667–1671.
73. Kim, J.M., Rasmussen, J.P., and Rudensky, A.Y. (2007). Regulatory T cells prevent catastrophic autoimmunity throughout the lifespan of mice. Nat. Immunol. *8*, 191–197.
74. Haribhai, D., Lin, W., Relland, L.M., Truong, N., Williams, C.B., and Chatila, T.A. (2007). Regulatory T Cells Dynamically Control the Primary Immune Response to Foreign Antigen. J. Immunol. *178*, 2961–2972.
75. Madisen, L., Zwingman, T.A., Sunkin, S.M., Oh, S.W., Zariwala, H.A., Gu, H., Ng, L.L., Palmiter, R.D., Hawrylycz, M.J., Jones, A.R., et al. (2010). A robust and high-throughput Cre reporting and characterization system for the whole mouse brain. Nat. Neurosci. *13*, 133–140.
76. Keir, M.E., Freeman, G.J., and Sharpe, A.H. (2007). PD-1 Regulates Self-Reactive CD8 + T Cell Responses to Antigen in Lymph Nodes and Tissues. J. Immunol. *179*, 5064–5070.
77. Schluns, K.S., Williams, K., Ma, A., Zheng, X.X., and Lefrançois, L. (2002). Cutting Edge: Requirement for IL-15 in the Generation of Primary and Memory Antigen-Specific CD8 T Cells. J. Immunol. *168*, 4827–4831.
78. Tafuri, A., Shahinian, A., Bladt, F., Yoshinaga, S.K., Jordana, M., Wakeham, A., Boucher, L.M., Bouchard, D., Chan, V.S., Duncan, G., et al. (2001). ICOS is essential for effective T-helper-cell responses. Nature *409*, 105–109.
79. Zhang, R., Huynh, A., Whitcher, G., Chang, J., Maltzman, J.S., and Turka, L.A. (2013). An obligate cell-intrinsic function for CD28 in Tregs. J. Clin. Invest. *123*, 580–593.
80. Polic, B., Kunkel, D., Scheffold, A., and Rajewsky, K. (2001). How αβ T cells deal with induced TCRα ablation. Proc. Natl. Acad. Sci. USA *98*, 8744–8749.
81. Patro, R., Duggal, G., Love, M.I., Irizarry, R.A., and Kingsford, C. (2017). Salmon provides fast and bias-aware quantification of transcript expression. Nat. Methods *14*, 417–419.
82. Bankhead, P., Loughrey, M.B., Fernández, J.A., Dombrowski, Y., McArt, D.G., Dunne, P.D., McQuaid, S., Gray, R.T., Murray, L.J., Coleman, H.G., et al. (2017). QuPath: Open source software for digital pathology image analysis. Sci. Rep. *7*, 16878.
83. Enot, D.P., Vacchelli, E., Jacquelot, N., Zitvogel, L., and Kroemer, G. (2018). TumGrowth: An open-access web tool for the statistical analysis of tumor growth curves. OncoImmunology *7*, e1462431.

STAR★METHODS

KEY RESOURCES TABLE

REAGENT or RESOURCE	SOURCE	IDENTIFIER
Antibodies		
CD8α (clone: 2.43)	BioXCell	Cat# BE0061; RRID: AB_1125541
ICOSL (clone: HK5.3)	BioXCell	Cat# BE0028; RRID: AB_1107566
IL-2 (clone: JES6-1A12)	BioXCell	Cat# BE0043; RRID: AB_1107702
IL-2 (clone: S4B6-1)	BioXCell	Cat# BE0043-1; RRID: AB_1107705
PD-1 (clone: 29F.1A12)	BioXCell	Cat# BE0273; RRID: AB_2687796
Rat IgG	Sigma	Cat# I8015; RRID: AB_1163629
B220 PE-Cy5 (clone: RA3-6B2)	BioLegend	Cat# 103210; RRID: AB_312995
Bcl-2 PE-Cy7 (clone: BCL/10C4)	BioLegend	Cat# 633511; RRID: AB_2565246
Bcl-xL Ax488 (clone: 54H6)	Cell Signaling Technology	Cat# 2767; RRID: AB_2274763
Bim PE (clone: C34C5)	Cell Signaling Technology	Cat# 12186; RRID: AB_2797842
CD107a (Lamp-1) Ax647 (clone: 1D4B)	BioLegend	Cat# 121610; RRID: AB_571991
CD11c Ax700 (clone: HL3)	BD Biosciences	Cat# 560583; RRID: AB_1727421
CD137 (4-1BB) PE (clone: 17B5)	BioLegend	Cat# 106105; RRID: AB_2205693
CD172a (Sirpα) FITC (clone: P84)	BioLegend	Cat# 144006; RRID: AB_11204425
CD25 APC (clone: PC61)	BioLegend	Cat# 102011; RRID: AB_312860
CD25 PE-Cy7 (clone: PC61)	BioLegend	Cat# 102015; RRID: AB_312864
CD26 BV711 (clone: H194-112)	BD Biosciences	Cat# 740678; RRID: AB_2740365
CD28 (clone: 37.51)	BioLegend	Cat# 102116; RRID: AB_11147170
CD3ε (clone: 145-2C11)	BioLegend	Cat# 100340; RRID: AB_11149115
CD4 BV605 (clone: RM4-5)	BioLegend	Cat# 100548; RRID: AB_2563054
CD44 BV421 (clone: IM7)	BioLegend	Cat# 103040; RRID: AB_2616903
CD45 APC-Cy7 (clone: 30-F11)	BioLegend	Cat# 103116; RRID: AB_312981
CD45.1 APC (clone: A20)	BioLegend	Cat# 110713; RRID: AB_313502
CD45.2 PerCP-Cy5.5 (clone: 104)	BioLegend	Cat# 109827; RRID: AB_893352
CD62L BV650 (clone: MEL-14)	BioLegend	Cat# 104453; RRID: AB_2800559
CD64 PE-Daz (clone: X54-5/7.1)	BioLegend	Cat# 139320; RRID: AB_2566559
CD80 PE-Cy7 (clone: 16-10A1)	BioLegend	Cat# 104734; RRID: AB_2563113
CD86 BV785 (clone: GL-1)	BioLegend	Cat# 105043; RRID: AB_2566722
CD8α BV785 (clone: 53-6.7)	BioLegend	Cat# 100749; RRID: AB_11218801
CTLA-4 APC (clone: UC10-4F10-11)	Millipore Sigma	Cat# MABF389; RRID: AB_2892076
F4/80 BV421 (clone: BM8)	BioLegend	Cat# 123137; RRID: AB_2563102
FcBlock (anti-mouse CD16/32) (clone: S17011E)	BioLegend	Cat# 156604; RRID: AB_2783138
Foxp3 PE (clone: FJK-16s)	Invitrogen	Cat# 12-5773-80; RRID: AB_465935
GITR PerCP-Cy5.5 (clone: DTA-1)	BioLegend	Cat# 126316; RRID: AB_2563384
Gr-1 PE-Cy5 (clone: RB6-8C5)	BioLegend	Cat# 108410; RRID: AB_313375
GzmB PE-CF594 (clone: GB11)	BD Biosciences	Cat# 562462; RRID: AB_2737618
H-2K^{b} PerCP-Cy5.5 (clone: AF6-88.5)	BioLegend	Cat# 116516; RRID: AB_1967133
IA/IE BV605 (clone: M5/114.15.2)	BioLegend	Cat# 107639; RRID: AB_2565894
ICOS Ax700 (clone: C398.4A)	Biolegend	Cat# 313527; RRID: AB_2566125
ICOS PE-Cy7 (clone: C398.4A)	BioLegend	Cat# 313520; RRID: AB_10643411
IFNγ PE-Daz (clone: XMG1.2)	BioLegend	Cat# 505846; RRID: AB_2563980
IL-2 PE (clone: JES6-5H4)	BioLegend	Cat# 503808; RRID: AB_315302
Ki67 FITC (clone: B56)	BD Biosciences	Cat# 556026; RRID: AB_396302
Mcl-1 Ax647 (clone: D2W9E)	Cell Signaling Technology	Cat# 78471; RRID: AB_2799914

(*Continued on next page*)

Continued

REAGENT or RESOURCE	SOURCE	IDENTIFIER
NK1.1 PE-Cy5 (clone: PK136)	BioLegend	Cat# 108716; RRID: AB_493590
pAKT$_{S473}$ BV421 (clone: M89-61)	BD Biosciences	Cat# 562599; RRID: AB_2737674
PD-1 APC (clone: 29F.1A12)	BioLegend	Cat# 135210; RRID: AB_2159183
PD-L1 APC (clone: 10F.9G2)	BioLegend	Cat# 124311; RRID: AB_10612935
pZap70$_{Y319}$ PE-Cy7 (clone: 1503310)	BioLegend	Cat# 683707; RRID: AB_2687048
TCRβ PE-Cy5 (clone: H59-597)	BioLegend	Cat# 109210; RRID: AB_313433
TNF FITC (clone: MP6-XT22)	BioLegend	Cat# 506304; RRID: AB_315425
XCR1 BV650 (clone: ZET)	BioLegend	Cat# 148220; RRID: AB_2566410
Zbtb46 PE (clone: U4-1374)	BD Biosciences	Cat# 565832; RRID: AB_2739372
Biological samples		
Paraffin-embedded sections of human melanoma	Providence Saint John's Health Center (Santa Monica, CA)	N/A
Chemicals, peptides, and recombinant proteins		
16% paraformaldehyde	Electron Microscopy Sciences	Cat# 15710
Brefeldin A Solution (1,000X)	BioLegend	Cat# 420601
Collagenase IV	Worthington	Cat# LS004189
Diphtheria Toxin	Calbiochem	Cat# 322326
DNAse I	Roche	Cat# 04536282001
FTY720	Cayman Chemical	Cat# 10006292
Lambda phosphatase	NEB	Cat#: P0753S
Mouse IL-2	BioLegend	Cat# 575404
Tamoxifen	Sigma	Cat# T5648
Critical commercial assays		
Foxp3 Transcription Factor Staining Buffer Set	Invitrogen	Cat# 00552300
NucView 488	Biotium	Cat# 10402
Deposited data		
Single-cell RNA sequencing, Sade-Feldman cohort	Sade-Feldman et al. 2018[13]	GEO: GSE120575
Bulk RNA expression data, Riaz cohort	Riaz et al. 2017[27]	GEO: GSE91061
Bulk RNA sequencing data, Gide cohort	Gide et al. 2019[28]	ENA: PRJEB23709
Bulk RNA sequencing data, Helmink cohort	Helmink et al. 2020[29]	EGA: EGAD00001005803
Experimental models: Cell lines		
mouse: D4M.3A	David Fisher (Massachusetts General Hospital and Harvard Medical School, Boston, MA), Lo et al. 2021[24]	RRID: CVCL_0P27
mouse: D4M.3A H2B SIINFEKL Cerulean (D4M-S)	Thorsten Mempel (Massachusetts General Hospital and Harvard Medical School, Boston, MA), Di Pilato et al. 2019[21]	N/A
mouse: MC38 cells	Kerafast	Cat# ENH204-FP; RRID: CVCL_B288
Experimental models: Organisms/strains		
mouse: B6.129(Cg)-Foxp3tm3(DTR/GFP)Ayr/J (*Foxp3^{DTR}*)	Jackson Laboratories	RRID: IMSR_JAX:016958
mouse: B6.129P2-Icos^{tm1Mak}/J (*Icos$^{-/-}$*)	Daniel Campbell (Benaroya Research Institute, Seattle, WA), Tafuri et al. 2001[78]	RRID: IMSR_JAX:004859
mouse: B6.Cg-Foxp3tm2Tch/J (*Foxp3^{GFP}*)	Jackson Laboratories	RRID: IMSR_JAX:006772
mouse: B6.Cg-Gt(ROSA)26Sortm14(CAG-tdTomato)Hze/J (*Rosa26$^{LSL\text{-}Tomato}$*)	Jackson Laboratories	RRID: IMSR_JAX:007914
mouse: B6.Cg-*Pdcd1$^{tm1.1Shr}$*/J (*Pdcd1$^{-/-}$*)	Jackson Laboratories	RRID: IMSR_JAX:028276
mouse: B6.SJL-*Ptprc^{a} Pepc^{b}*/BoyJ (B6 CD45.1)	Jackson Laboratories	RRID: IMSR_JAX:002014
mouse: C57BL/6-Tg(Cd8a-cre)1Itan/J (*E8I^{cre}*)	Jackson Laboratories	RRID: IMSR_JAX:008766

(*Continued on next page*)

Continued

REAGENT or RESOURCE	SOURCE	IDENTIFIER
mouse: C57BL/6J	Jackson Laboratories	RRID: IMSR_JAX:000664
mouse: *Cd28*$^{f/f}$	Laurence Turka (Massachusetts General Hospital and Harvard Medical School, Boston, MA), Zhang et al. 2013[79]	N/A
mouse: Foxp3tm9(EGFP/cre/ERT2)Ayr/J (*Foxp3*^{creERT2})	Jackson Laboratories	RRID: IMSR_JAX:016961
mouse: *Il2*^{GFP}	Casey Weaver (University of Alabama, Birmingham, AL), DiToro et al. 2018[39]	N/A
mouse: *Pdcd1*$^{f/f}$	Shimon Sakaguchi (University of Osaka, Japan), Kamada et al. 2019[14]	N/A
mouse: *Rosa26*$^{LSL\text{-}Salsa6f}$	Michael Cahalan (University of California, Irvine, CA), Dong et al. 2017[34]	RRID: IMSR_JAX:031968
mouse: *Trac*$^{f/f}$	Klaus Rajewsky (Max Delbrück Center, Berlin, Germany), Polic et al. 2001[80]	N/A
Software and algorithms		
FCS Express 7	*De Novo* Software	https://denovosoftware.com/
ImageJ 1.53t	Freeware/NIH	https://imagej.nih.gov/ij/
Imaris 9.7.2	Bitplane	http://www.bitplane.com
Matlab R2021b	Mathworks	https://www.mathworks.com/products/matlab.html
Prism 10	GraphPad	https://www.graphpad.com
Salmon	Patro et al. 2017[81]	https://combine-lab.github.io/salmon/
CellChat analysis scripts	This paper	https://doi.org/10.5281/zenodo.11122613
Imaris add-on to randomize cell positions	This paper	https://doi.org/10.5281/zenodo.11122613
MATLAB cell motility analysis scripts	This paper	https://doi.org/10.5281/zenodo.11122613
QuPath	Bankhead et al. 2017[82]	https://qupath.github.io/
Other		
AccuCheck flow cytometry counting beads	Invitrogen	Cat# PCB100
Matrigel	Corning	Cat# CB40230A
Zombie Yellow Fixable Viability Kit	BioLegend	Cat# 423104

RESOURCE AVAILABILITY

Lead contact

Further information and requests for resources and reagents should be directed to and will be fulfilled by the lead contact, Francesco Marangoni (f.marangoni@uci.edu).

Materials availability

This study did not generate new unique reagents.

Data and code availability

- This paper analyzes existing, publicly available bulk and single-cell RNA sequencing data. The datasets' accession numbers are listed in the key resources table. Microscopy data reported in this paper will be shared by the lead contact upon request.
- All original code has been deposited at GitHub / Zenodo and is publicly available as of the date of publication. DOIs are listed in the key resources table.
- Any additional information required to reanalyze the data reported in this paper is available from the lead contact upon request.

EXPERIMENTAL MODEL AND STUDY PARTICIPANT DETAILS

Cells

D4M.3A (D4M) and D4M.3A H2B SIINFEKL Cerulean (D4M-S) melanoma cells were obtained from David Fisher and Thorsten Mempel (Massachusetts General Hospital and Harvard Medical School, Boston, MA), respectively, and grown in DMEM supplemented with 10% fetal calf serum (GeminiBio) under 37°C / 5% CO_2 conditions. These cell lines are derived from male mice[20] and have not been authenticated. MC38 colon carcinoma cells were purchased from Kerafast (Cat# ENH204-FP) and grown in DMEM supplemented with 10% fetal calf serum (GeminiBio) under 37°C / 5% CO_2 conditions. MC38 cells are derived from female mice. This cell line has not been authenticated. All cell lines were routinely tested for mycoplasma contamination and found negative.

Mice

E8I^{cre},[71] *Foxp3*^{creERT2},[72] *Foxp3*^{DTR},[73] *Foxp3*^{GFP},[74] *Rosa26*$^{LSL\text{-}Tomato}$,[75] *Pdcd1*$^{-/-}$[76] CD45.1,[77] and C57BL/6 mice were purchased from The Jackson Laboratory. *Icos*$^{-/-}$[78] bone marrow was obtained from the laboratory of Daniel Campbell (Benaroya Research Institute, Seattle, WA). *Cd28*$^{f/f}$,[79] *Il2*^{GFP},[39] *Pdcd1*$^{f/f}$,[14] *Rosa26*$^{LSL\text{-}Salsa6f}$,[34] and *Trac*$^{f/f}$[80] mice were obtained from the investigators who generated them. Mice were enrolled in experiments at 8-20 weeks of age. D4M and D4M-S melanomas were studied in both male and female mice. The MC38 experiments reported here were conducted in male mice. Mice were bred, housed, enrolled in experiments, and euthanized according to protocols approved by the Institutional Animal Care and Use Committee (IACUC) of the University of California Irvine and the Massachusetts General Hospital.

Melanoma specimens

The study was approved by the Ethics Committee at Saint John's Cancer Institute (MORD-RTPCR-0995) and follows the Declaration of Helsinki. The samples were used after obtaining informed consent from the patients. The patients underwent surgery and were diagnosed with metastatic melanoma at the Providence Saint John's Health Center. The quality of all formalin-fixed-paraffin-embedded (FFPE) sections was evaluated using hematoxylin and eosin staining. All FFPE sections included in the study were reviewed by a board-certified specialist pathologist at the Surgery Pathology Department of Saint John's Health Center. The clinical and pathological information data of the resected specimens analyzed from each patient (one male, two female) are described in Figure S6A. FFPE-embedded resected metastatic tissue was sectioned (5 μm) and mounted on poly-L-lysine coated superior adhesive slides (Leica #3800080). Immunofluorescence detection of GP100, CD45, CD8, FOXP3, and ICOS signals was performed through the PhenoCycler technology (outsourced to Akoya Biosciences).

METHOD DETAILS

Analysis of existing human datasets

Determination of Treg abundance in melanoma was conducted by selecting patients i) treated with PD-1 monotherapy only and ii) for whom pre-treatment and on-treatment data were available. Treg quantification in the Sade-Feldman dataset directly reflected the percentage for cluster G7 (Tregs) reported in Sade-Feldman dataset of the original paper.[13] If a patient had multiple biopsies taken on-treatment, the Treg level was averaged. For the Huang dataset,[30] we directly calculated the percentage of melanoma patients experiencing tumor-Treg accumulation after PD-1 immunotherapy from Figure 4A of the original publication. To measure Treg abundance in bulk RNA sequencing datasets,[27–29] we quantified the transcripts per million (TPM) for the GENCODE 32 GRCh38 genes using Salmon v1.9.0.[81] Treg cell abundance was inferred from the expression of *FOXP3*.

Cell-cell signaling pathways were analyzed using the R package CellChat.[48] The CellChat package contains a manually curated database of ligand-receptor (L-R) interactions for the human and mouse species. CellChat receives as input the single-cell expression data as well as the cell type annotations for each cell and computes a "communication score" for every combination of sender cell type and receiver cell type and for each L-R interaction. The count matrix and cell type annotations, split into pre-treatment and post-treatment groups, are taken from the original publication.[13] The original data were further filtered for treatment, and only patients who received PD-1 monotherapy were maintained (12 biopsies pre-treatment, 17 post-treatment, 10,609 cells total). The CellChat pipeline is first performed separately on the pre-treatment and post-treatment groups to compute the communication probabilities, as described in.[48] CellChat also calculates *p* values for each interaction over each pair of cell types by performing permutation tests. Interactions were tested at a 5% significance level to identify cell types sending and receiving IL-2 signaling in the post-treatment group. Further analyses focused on the signaling from *TCF7*-expressing memory to Treg cells (group 10 to group 7 in ref.[13]), the only pair for which such signaling was identified. To quantify the change in IL-2 signaling in pre-treatment versus post-treatment conditions, we computed the fold change of the communication score and performed differential expression analysis of *IL-2* in the *TCF7*-expressing memory T cells before and after therapy. We used the Mann-Whitney U test to reveal statistical differences in the differential expression analysis.

Antibody treatment of tumor-bearing mice

Mice received a subcutaneous injection of 10^6 D4M cells, $2x10^6$ D4M-S cells, or 10^6 MC38 cells. D4M-S and MC38 cells were resuspended in Matrigel to facilitate engraftment. To maximize material for downstream analyses, we injected two tumors per mouse 1 cm off the midline in both sides of the abdomen. In studies involving the deletion of floxed genes in *Foxp3*^{creERT2} models, tamoxifen

treatment consisted of oral gavage (15 mg in 75 μl EtOH + 425 μl corn oil) on day 5 followed by four i.p. daily injections of 2 mg (in 10 μl EtOH + 40 μl corn oil). Six days before sacrifice, 200 μg αPD-1 (29F.1A12) was injected with 1 mg/kg FTY720 i.p., and injections were repeated every other day. FTY720 blocks the egress of lymphocytes from secondary lymphoid organs, allowing us to study the effect of PD-1 blockade on an isolated tumor environment. IL-2 neutralization was performed by injecting 750 μg of S4B6-1 and 750 μg of JES6-1A12 i.v. every three days to block interaction with the α and β subunits of the IL2R. In studies using IL-2 immunocomplexes, 5 μg of IL-2 antibodies (JES6-1A12) were mixed with 0.5 μg per mouse of recombinant IL-2 and incubated at 37°C for 15 minutes. IL-2 immunocomplexes were injected every two days to trigger Treg expansion. αCD8 (2.43) and αICOSL (HK5.3) were administered every three days at a dose of 300 μg i.p. We injected rat IgG as an isotype control through the same route and at the same concentration as each antibody.

Measurement of immunotherapy-treated tumors

In experiments to investigate the kinetics of tumor growth, we implanted only one tumor. For concomitant PD-1 and ICOSL blockade, 200 μg αPD-1 antibodies were administered every two days and 300 μg αICOSL antibodies every three days, beginning from day 13 after tumor implant. For sequential immunotherapy, αICOSL was injected on days 6 and 9 after tumor implantation, while αPD-1 antibodies were started on day 12 and given every two days. Tumors were measured three times a week with an electronic caliper, and tumor volume was estimated using the formula 0.5 x a x b^2, where a is the maximum and b is the perpendicular tumor diameter. Immunotherapy administration was stopped when all mice either controlled the tumor or reached an endpoint as per our IACUC protocol. Mice were sacrificed when tumors reached a maximum diameter >15 mm or both diameters >10 mm.

Diphtheria toxin treatment

In studies where Tregs were partially depleted, *Foxp3*^{DTR} mice received two D4M-S tumors and were treated with FTY720, αPD-1, and diphtheria toxin (Calbiochem) i.p. starting from day 12 and every other day after that. We titrated the amount of diphtheria toxin to 500 pg/g to decrease Treg counts to the levels observed without PD-1 inhibition. *Icos*$^{-/-}$:*Foxp3*^{DTR} bone marrow chimeras received a fully-ablative DT treatment: 25 μg/kg on the first day, followed by 5 μg/kg daily afterward.[15] Upon sacrifice, tumors were weighed and analyzed by flow cytometry.

Bone marrow chimeras

We created bone marrow chimeras by irradiating mice at 950 rads (γ-rays source) or 800 rads (X-rays source). Irradiation doses were established to ensure engraftment of 8-10 x 10^6 donor bone marrow cells with minimal lethality. To assess the role of PD-1 in the transition between cTreg to eTreg to tumor-Treg cells, we injected a mixture of CD45.2$^+$ *Pdcd1*$^{-/-}$ and CD45.1$^+$ bone marrow into 950-rad irradiated CD45.1 mice. To elucidate the direct effect of ICOS signaling on tumor-Treg accumulation after PD-1 blockade, we injected a mixture of *Foxp3*^{DTR} and either WT or *Icos*$^{-/-}$ marrow into 800-rad irradiated *Foxp3*^{DTR} hosts. We titrated bone marrow mixtures to produce a 1:1 ratio within Treg cells. Bone marrow chimeras were enrolled in experiments two months after transplantation to ensure hematopoietic reconstitution. We confirmed engraftment by flow cytometry analysis of blood.

Flow cytometry

Tumor cell suspensions were prepared by digestion of finely minced tissue for 30 min at 37°C using DMEM 10% FCS supplemented with 1.5 mg/ml Collagenase IV (Worthington) and 50 U/ml DNAse I (Roche). Tumor-draining lymph nodes were mechanically dissociated. All cell preparations were filtered.

We stained 8x10^6 cells except otherwise stated. Dead cells were stained through exposure to Zombie Yellow (1:200), diluted in PBS, for 15 min at 4°C. We determined absolute cell numbers using AccuCheck flow cytometry counting beads (Invitrogen). Cells were subsequently treated with 5 μg/ml FcBlock for 10 min at 4°C to decrease nonspecific Ab binding. Extracellular antibody staining was carried out at 4°C for 20 minutes in FACS buffer (PBS 0.5% BSA, 2 mM EDTA). Cells were then permeabilized using the Foxp3 fixation-permeabilization buffer (Invitrogen), while intracellular staining was performed at 4°C for 30 min in Foxp3 wash buffer. We acquired the samples on a NovoCyte Quanteon flow cytometer and analyzed the data using FCS Express.

T cell activation panel

The panel to count T cells and analyze their activation included Zombie Yellow and αCD45, αCD8, αCD4, αFoxp3, αCD44, αCD62L, and antibodies against various activation markers including αKi67, αICOS, αGITR, α-granzyme B, αLamp-1, and αCTLA-4.

Apoptosis regulators panel

We stained cells with a panel including Zombie Yellow and αCD45, αCD8, αCD4, αFoxp3, αCD44, αCD62L, αKi67, and antibodies against various controllers of apoptosis including αBim, αBcl-xL, αBcl-2, αMcl-1, and αICOS.

Cytokine panel

To measure cytokine production by T cells, 4 x 10^6 live cells from tumor-draining lymph nodes or tumors were stimulated with plate-bound αCD3ε (10 μg/ml) and αCD28 (10 μg/ml) in the presence of brefeldin A (5 μg/ml) for eight hours at 37°C. Cells were stained using Zombie Yellow and αCD45, αCD8, αCD4, αFoxp3, αCD44, αIFNγ, αTNF, and αIL-2 antibodies.

APC panel

To assess APC activation and numbers, we stained cells with a panel including Zombie Yellow, a lineage cocktail of antibodies against TCRβ, Gr-1, B220, and NK1.1, as well as αCD45, αCD64, αF4/80, αH-2K^b (MHC-I), αIA/IE (MHC-II), αCD26, αCD11c, αXCR1, αCD172a (Sirpα), αCD80, αCD86, αPD-L1 (not binding CD80), and αZbtb46 antibodies. After gating for live CD45$^+$ Lin$^-$

IA/IE$^+$ cells, TAMs were gated as CD64$^+$ F4/80$^+$. From the CD64$^-$ F4/80$^-$ population, DCs were identified as CD26$^+$ Zbtb46$^+$ and further gated into DC1s (Sirpα^- XCR1$^+$) and DC2s (Sirpα^+ XCR1$^-$).

Apoptosis Kit

To evaluate apoptosis in tumor lymphocytes, we stained 16x10^6 cells (in two wells) for D4M tumors or 8x10^6 cells for D4M-S tumors. Cells were stained with Zombie Yellow and αCD44, αCD4, αCD62L, αCD8, αCD45, αCD137 (4-1BB), and αCD25. Surface staining of CD137 and CD25 staining was necessary to identify tumor-Tregs without fixation/permeabilization,[16] which is incompatible with active caspase-3/7 detection. We then stained for caspase-3/7 activity using NucView 488 according to the manufacturer's protocol.

Phospho-flow

Tumors and tdLNs were harvested for phospho-flow staining and kept on ice. To achieve immediate fixation and dissociation, tumors were placed in DMEM 10% FCS containing 1.5 mg/ml Collagenase IV (Worthington), 50 U/ml DNAse I (Roche), and 4% formaldehyde, dissociated with the gentleMACS program "tumor 01-01", and incubated at 37°C for 15 minutes. Tumors were dissociated again with the gentleMACS program "tumor 01-01", and samples were filtered using a 40μm cell strainer. Draining lymph nodes were mechanically dissociated in 3 ml DMEM 10% FCS, filtered through a 40 μm mesh, and fixed through the direct addition of 1 ml of 16% formaldehyde (thus, final formaldehyde concentration is 4%) and incubation for 15 minutes at 37°C. Cells were then permeabilized with ice-cold methanol added dropwise while vortexing, and incubated for 20 minutes on ice. To generate controls with no phosphorylated epitopes, we incubated a 50 μl aliquot of some samples with 8 IU lambda phosphatase at 30°C for 45 minutes. Cells were plated 4x10^6 per well and treated with 5 μg/ml FcBlock for 10 min at room temperature. Staining with αCD45 (0.5 μg/ml), αCD4 (0.5 μg/ml), αCD8 (0.5 μg/ml), αFoxp3 (4 μg/ml), αpZap70$_{Y319}$ (0.24 μg/ml), αpAKT$_{S473}$ (0.5 μg/ml), was performed in PBS 0.5% BSA for 1 hour at room temperature.

Preparation of mice for F-IVM studies

We induced Salsa6f expression in Tregs by treating *Foxp3^{creERT2}xRosa26$^{LSL\text{-}Salsa6f}$* mice with three 10 mg tamoxifen gavages (in 50 μl EtOH + 450 μl corn oil) spaced two days apart. Subsequently, mice were epilated by shaving and a brief application of hair remover cream. 7.5 x 10^5 D4M-S cells (resuspended in 10 μl of PBS) were injected in the center of the back, approximately 1 cm to the right of the midline. Seven to eight days after tumor injection, we surgically implanted a dorsal skinfold chamber (DSFC) such that the tumor was centered in the optical window of the DSFC. Analgesia was achieved by injecting 5 mg/kg carprofen s.c. pre-operatively and every 24 hours after that. Two control groups were generated and later pooled due to similar results: mice imaged before administration of αPD-1 or 24 h after injection of isotype control antibodies. These control groups were compared to mice imaged 24 h after treatment with αPD-1.

F-IVM time-lapse recordings

Mice were anesthetized with inhaled isoflurane. To prevent blurring artifacts due to respiratory and other physiologic movements, the DSFC was secured to the motorized stage using a custom-built platform. The DSFC was maintained at 37° ± 0.5°C utilizing a heating system (Warner Instruments) and a thermocouple-based temperature sensor placed next to the tissue. Mice were imaged using a Leica SP8 DIVE upright multiphoton microscope fitted with a Leica 25x water-immersion objective with a correction collar (HC IRAPO, NA = 1.0, WD = 2.6 mm). Insight X3 laser was tuned to 950 nm for optimal excitation of GCaMP6f and Tomato. For four-dimensional recordings of cell migration and signaling, stacks of 9 optical sections (X=350 μm, Y=350 μm; 512 x 512 pixels) with 4 μm z-spacing were acquired every 5 seconds to provide imaging volumes of 32 μm in depth per time point (voxel size 0.69 μm x 0.69 μm x 4 μm). Imaging depth was typically 30-120 μm below the DSFC glass. We detected emitted fluorescence and second harmonic signals as follows: PMT channel one bandwidth 465 – 486nm; HyD channel two bandwidth 490 – 545 nm; PMT channel three bandwidth 560 – 600nm. Datasets were imported in Imaris 9.7 (Bitplane) for analysis, generation of maximum intensity projections, and exporting as MPEG-4 movies.

Analysis of cell motility and Salsa6f signaling

Image processing was performed using Imaris and Fiji plugins (version 1.53t). The threshold cutoff module was used to remove diffuse backgrounds for each channel, and then a Gaussian smoothing of the 0.8-pixel radius was applied to the entire image. TdTomato (red channel) photobleaching was corrected using the CorrectBleach plugin (Fiji) using the histogram matching method, and the noise was reduced using the "Remove Outliers" filter with a radius of two pixels and two standard deviations. Tomato$^+$ cells were tracked using the "spot" function of Imaris 9.7 (Bitplane) to obtain XYZ coordinates. To measure Ca^{2+}, we used green channel intensities rather than the typical Green/Red ratios to avoid potential red-channel intensity artifacts induced by the bleach correction algorithm. Ca^{2+} signaling was quantified through the mean fluorescence of the GFP (green, GCaMP6f) channel. We calculated the baseline green fluorescence for each track as a band centered on the 30th percentile of fluorescence and having as extremes the difference between the 30th percentile and the minimum fluorescence value. Thus, the upper limit of the baseline is (2 x 30th percentile – minimum) of green channel fluorescence. This value was subtracted from all GFP fluorescence measurements to highlight fluorescence values above baseline. Subsequently, signaling track segments were identified based on the following characteristics: i) GFP signal above the baseline for at least 15 seconds; ii) segments shorter than one minute must have an AUC >1000; and iii) segments longer than one minute must have an AUC/duration ratio >800. These characteristics were established empirically so that automatically identified signaling segments matched with visually annotated ones on a subset of the data. We extracted the

percentage of time a track is signaling, the maximum signaling peak fluorescence, signaling duration, and peak AUC using Matlab (Mathworks).

Analysis of CD8$^+$ T cell:Treg colocalization in mouse and human melanomas

Mouse samples

We implanted D4M-S tumors in *Foxp3*^{GFP}x*E8I*^{cre}x*Rosa26*$^{LSL\text{-}Tomato}$ mice and harvested them for tissue-wide imaging after 11-14 days. Following euthanasia, tumors were carefully dissected and fixed onto a plastic coverslip using tissue adhesive (3M Vetbond). Explants were fixed overnight in 4% paraformaldehyde, washed at least ten times with PBS, and imaged within 30 days. For fluorophore excitation, we tuned the Insight X3 laser to 950 nm. Detection parameters were as follows: PMT channel one bandwidth 406 – 485nm; HyD channel two bandwidth 499 – 536nm; PMT channel three bandwidth 560 – 620nm. Individual 3D image stacks (X= 590 μm, Y= 590 μm, Z= 400-500 μm) were collected with a voxel size of 1.15 μm x 1.15 μm x 5 μm. 3D Image blocks were stitched using the Leica "merge" algorithm (10% overlap) to generate the montage images. To assess whether CD8$^+$ T cells and Tregs co-localized in montage images, we identified CD8$^+$ T cells and Tregs using the Imaris "spot" function and measured the distance of each Treg to the closest CD8$^+$ T cell by the Imaris distance transformation algorithm. We then generated a surface that includes all the tumor-associated T cells and randomized Treg positions within the surface boundaries. The distance between randomized Treg cells and the closest CD8$^+$ T cell was again determined by the Imaris distance transformation algorithm.

Human samples

Images provided by Akoya Biosciences were opened in QuPath[82] and single channels were exported as .tiff files. We subsequently reconstructed the image in Imaris for further analysis. We identified CD8$^+$ T cells through the "spot" function and defined CD8$^+$ T cell clusters by applying a nearest-neighbor algorithm (average of nearest nine CD8$^+$ T cells ranging from 30 to 60 μm). Finally, the distance of each Treg cell from the nearest CD8$^+$ T cell cluster was measured before and after their randomization within the space occupied by CD45$^+$ cells.

QUANTIFICATION AND STATISTICAL ANALYSIS

The numbers of individual cells, recordings, and animals analyzed are indicated in the figure legends. Two-tailed Mann-Whitney U test or Student's t test (in case of normal or lognormal distributions) were used to compare two groups. To analyze tumor growth curves, we used type II Anova followed by Holm post-test, as indicated in ref.[83] The chi-squared test was used for categorical variables. We compared distributions using the non-parametric Kolmogorov–Smirnov test. All statistical tests were performed using Prism 10 (GraphPad). *p* values smaller than 0.05 were considered statistically significant.